Portland State University

PDXScholar

Geology Faculty Publications and Presentations | Geology

3-2017

Ground-Rupturing Earthquakes on the Northern Big Bend of the San Andreas Fault, California, 800 A.D. to Present

Katherine Scharer
U.S. Geological Survey

Ray J. Weldon II
University of Oregon

Glenn Biasi
University of Nevada, Reno

Ashley Streig
Portland State University, streig@pdx.edu

Thomas Fumal
U.S. Geological Survey

Follow this and additional works at: https://pdxscholar.library.pdx.edu/geology_fac

 Part of the Geology Commons, Geophysics and Seismology Commons, and the Tectonics and Structure Commons

Let us know how access to this document benefits you.

Citation Details

Scharer, K., R. Weldon II, G. Biasi, A. Streig, and T. Fumal (2017), Ground-rupturing earthquakes on the northern Big Bend of the San Andreas Fault, California, 800 A.D. to Present, J. Geophys. Res. Solid Earth, 122, 2193–2218 doi:10.1002/ 2016JB013606

This Article is brought to you for free and open access. It has been accepted for inclusion in Geology Faculty Publications and Presentations by an authorized administrator of PDXScholar. Please contact us if we can make this document more accessible: pdxscholar@pdx.edu.

AGU PUBLICATIONS

JGR

Journal of Geophysical Research: Solid Earth

RESEARCH ARTICLE
10.1002/2016JB013606

Key Points:
- Eleven paleoearthquake records of ground-rupturing earthquakes fill 200 km long gap in records along the southern San Andreas Fault
- Average interval length between paleoearthquakes in last 1200 years is ~100 years, and individual intervals range from ~22 to 186 years
- Paleoenvironmental data and radiocarbon dating show that Big Bend and Mojave sections rupture together ≥ 50% of the time in major earthquakes

Supporting Information:
- Supporting Information S1
- Supporting Information S2

Correspondence to:
K. Scharer,
kscharer@usgs.gov

Citation:
Scharer, K., R. Weldon II, G. Biasi, A. Streig, and T. Fumal (2017), Ground-rupturing earthquakes on the northern Big Bend of the San Andreas Fault, California, 800 A.D. to Present, *J. Geophys. Res. Solid Earth*, *122*, 2193–2218 doi:10.1002/2016JB013606.

Received 30 SEP 2016
Accepted 19 FEB 2017
Accepted article online 2 MAR 2017
Published online 22 MAR 2017

©2017. American Geophysical Union. All Rights Reserved.

Ground-rupturing earthquakes on the northern Big Bend of the San Andreas Fault, California, 800 A.D. to Present

Katherine Scharer[1], Ray Weldon II[2], Glenn Biasi[3], Ashley Streig[4], and Thomas Fumal[1]

[1]Earthquake Science Center, U.S. Geological Survey, Pasadena, California, USA, [2]Department of Earth Sciences, University of Oregon, Eugene, Oregon, USA, [3]Nevada Seismological Laboratory, University of Nevada, Reno, Nevada, USA, [4]Department of Geology, Portland State University, Portland, Oregon, USA

Abstract Paleoseismic data on the timing of ground-rupturing earthquakes constrain the recurrence behavior of active faults and can provide insight on the rupture history of a fault if earthquakes dated at neighboring sites overlap in age and are considered correlative. This study presents the evidence and ages for 11 earthquakes that occurred along the Big Bend section of the southern San Andreas Fault at the Frazier Mountain paleoseismic site. The most recent earthquake to rupture the site was the M_w7.7–7.9 Fort Tejon earthquake of 1857. We use over 30 trench excavations to document the structural and sedimentological evolution of a small pull-apart basin that has been repeatedly faulted and folded by ground-rupturing earthquakes. A sedimentation rate of 0.4 cm/yr and abundant organic material for radiocarbon dating contribute to a record that is considered complete since 800 A.D. and includes 10 paleoearthquakes. Earthquakes have ruptured this location on average every ~100 years over the last 1200 years, but individual intervals range from ~22 to 186 years. The coefficient of variation of the length of time between earthquakes (0.7) indicates quasiperiodic behavior, similar to other sites along the southern San Andreas Fault. Comparison with the earthquake chronology at neighboring sites along the fault indicates that only one other 1857-size earthquake could have occurred since 1350 A.D., and since 800 A.D., the Big Bend and Mojave sections have ruptured together at most 50% of the time in $M_w \geq 7.3$ earthquakes.

1. Introduction

In southern California, the Carrizo, Big Bend, and Mojave sections of the southern San Andreas Fault (SSAF; Figure 1) accommodate the majority (50–70%) of plate motion and thus represent the highest seismic hazard for the region [*Johnson et al.*, 2007; *Field et al.*, 2015]. For this reason, these sections of the SSAF, which last ruptured in the historic Fort Tejon earthquake of 1857, have been the focus of detailed paleoseismic investigations to understand the timing, extent, and magnitude of prehistoric earthquakes. Due to the short historic record in the region, considered complete since ~1800 A.D. [*Toppozada et al.*, 2002], a principle area of focus is the recurrence behavior of the fault as determined from paleoseismic records of ground-rupturing earthquakes. Two sites on the Mojave section, Pallett Creek and Wrightwood (Figure 1), provide the longest records for the SSAF, both with over 10 paleoearthquake ages determined from radiocarbon dating of faulted sediments [*Sieh et al.*, 1989; *Biasi et al.*, 2002; *Fumal et al.*, 2002; *Scharer et al.*, 2007]. Using these paleoearthquake chronologies, subsequent studies examined the statistical behavior of earthquake recurrence at each site using parameters such as the average interval between earthquakes, the coefficient of variation (COV) of each chronology, and nonparametric tests for clustering and periodicity [*Biasi et al.*, 2002; *Scharer et al.*, 2010, 2011]. These studies found that the sites on the Mojave section of the SSAF have an average interval ranging from 100 to 135 years and a COV of ~0.6, indicating quasiperiodic behavior; statistical tests of each earthquake chronology indicate that neither site exhibits clustering that is greater than would be expected from a random distribution.

Other research has focused on the magnitude of paleoearthquakes recorded along the SSAF. One approach to determine magnitude is to use geomorphic features such as gullies and small channels that are offset along the fault to estimate the amount of displacement accumulated in successive earthquakes [*Sieh*, 1978; *Zielke et al.*, 2010]. *Zielke et al.* [2012] measured dozens of offset features along the 350 km long 1857 rupture and calculated an M_w of 7.7 for that historic earthquake based on the slip distribution. To extend this approach back in time is challenging, as gully incision events along the reach of the fault must be more

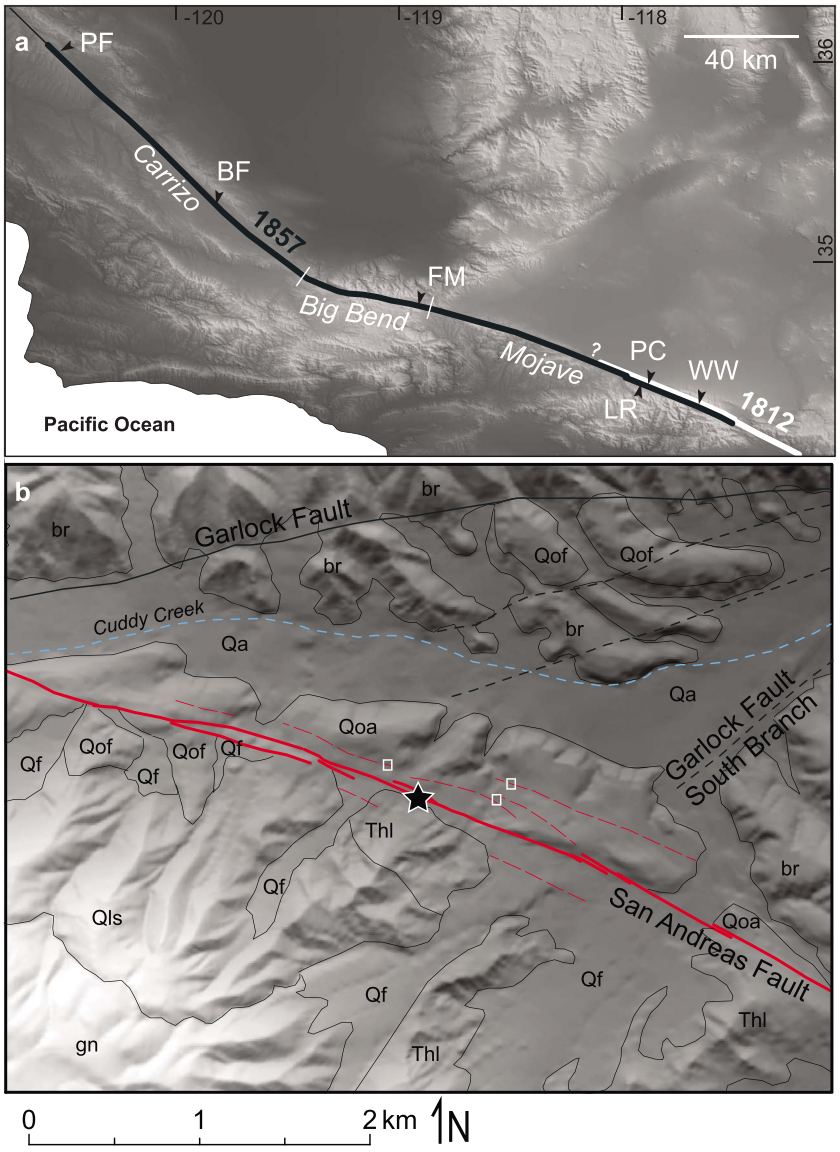

Figure 1. (a) Digital elevation model (DEM) of southern California identifying rupture extent of historic 1857 (black) and 1812 (white) earthquakes on the SSAF and key paleoseismic sites (PF: Parkfield, BF: Bidart Fan, FM: Frazier Mountain, LR: Littlerock, PC: Pallett Creek, WW: Wrightwood). Elevation data derived from USGS National Elevation Data Set, 1/3 arcsec. (b) Simplified geologic map of area around Frazier Mountain paleoseismic site (star) on 10 m DEM. SAF traces are based on geomorphology from the lidar; the small white boxes show location of three trenches we completed that show either minor Holocene cracking or no evidence of ground-rupture, indicating that the dashed faults are not significant. Garlock Fault strands (thick black lines) and geologic units simplified and modified from *Crowell* [2003] and *Swanson and Olson* [2016]. Qa: young alluvium; Qf: young alluvial fan deposits; Qls: landslide; Qoa: Pleistocene terraces of *Zhou* [1990]; Qof: old alluvial fan deposits; Thl: Pliocene Lower Hungry Valley Formation (locally landslide); gn: Paleo-Proterozoic gneiss of Frazier Mountain; br: undifferentiated bedrock.

frequent than earthquakes and the gullies must be minimally modified and well preserved. Lack of sufficient offset features has hampered robust estimates of slip-per-event prior to the 1857 rupture [*Akçiz et al.*, 2010; *Zielke et al.*, 2015; *Scharer et al.*, 2016].

An alternate approach to estimating paleoearthquake magnitude is to build rupture histories based on earthquake chronologies (and if available, displacement) from several paleoseismic trench sites, assuming that contemporaneity of paleoearthquakes at neighboring sites indicates a rupture that spans both locations. These studies have generally concluded that the rupture extent and thus magnitude of paleoearthquakes from the Carrizo through the Mojave section of the SSAF are not uniform, but instead show variations

consistent with a range of moderate to large magnitudes [*Sieh*, 1996; *Weldon et al.*, 2004; *Biasi and Weldon*, 2009; *Akçiz et al.*, 2010; *K. Scharer et al.*, 2014].

This study evaluates the rupture history of the SSAF utilizing a new long record from the Frazier Mountain paleoseismic site (Figure 1). The site is important for understanding the behavior of the SSAF for two reasons. First, the style of deformation and high sedimentation rate at the site result in a large number of robust observations of ground rupture and the ability to discriminate and date individual earthquake horizons, resulting in a long record of individual earthquakes. It is the first long record on the Big Bend of the SSAF and thus provides an independent estimate of earthquake recurrence for comparison to the long records on the Mojave section. Second, the site is located midway along a 200 km stretch of the fault along which there are no other sites with more than a couple of paleoearthquake observations. Thus, the Frazier Mountain site helps to bridge data along the SSAF that is important for evaluating spatial rupture patterns over time and for exploring the magnitude distribution of earthquakes on the SSAF important in seismic hazards [e.g., *Field et al.*, 2015].

This work builds on several publications that describe paleoseismic investigations at the Frazier Mountain paleoseismic site. *Lindvall et al.* [2002] described the first trench excavated at the site (Trench 1; T1) and identified evidence for two earthquakes in the upper meter of deposits. We subsequently re-excavated T1 in a series of excavations, herein called cuts, which both deepened and widened the original footprint of T1, and also dug a network of more than 20 additional trenches to document the earthquake history and deformation at the site (Figure 2). Complete photomosaic trench logs and detailed descriptions of the stratigraphy and deformation revealed in T1 are publically available in *K. M. Scharer et al.* [2014, 2015]. Line drawings of the T1 cuts are provided in Figure S1 in the supporting information. *K. Scharer et al.* [2014] focused on the history of the site since ~1350 A.D., providing a summary of radiocarbon dates and paleoearthquake ages, and examined the Frazier Mountain site in the context of how ground-rupturing earthquakes on the Big Bend section may correlate with ruptures observed on the Mojave and Carrizo sections of the SSAF. Minor modifications to the previous studies are noted in relevant sections of the text. This paper combines and synthesizes observations from these publications, provides radiocarbon dates for the full stratigraphic section and all the earthquakes from the site, and explores the statistics and spatial patterns of earthquake recurrence along the Big Bend section of the SSAF.

2. Geologic Setting and Site Description

The Frazier Mountain paleoseismic site is located along the northern flank of Frazier Mountain (Figure 1b), a 2450 m high, broad peak composed of Precambrian biotite gneiss. Deposits at the site are sourced primarily from two catchments on the northeast edge of Frazier Mountain that drain a Quaternary landslide in the gneissic unit and nonmarine sandstone and mudstone of the Pliocene Hungry Valley Formation [*Crowell*, 2003; *Swanson and Olson*, 2016]. To the north, the site is isolated from Cuddy Creek by a set of Pleistocene alluvial fan deposits (Qoa) that have been translated from the northwest [*Zhou*, 1990]. The site is located about 4 km southeast of the intersection of the main strand of the Garlock Fault with the SSAF and 1.5 km west of an inferred South Branch of the Garlock Fault, which is thought to be inactive (Figure 1b). Neither strand of the Garlock shows offset of the Qoa deposits [*Swanson and Olson*, 2016].

The excavations are located within an 80 m wide by 330 m long, fault parallel closed basin that sits between the low hills consisting of Qoa and the northwest flank of Frazier Mountain (Figure 2). Most of the sediment at the site is supplied by a broad, relatively planar alluvial fan (Qyf) on the northwest end of the basin (Figure 2a). At the southeast end of the basin, outflow is restricted by a small alluvial fan that separates the basin from a channel incised across the Qoa surface. The basin is an ephemeral pond; it was partially filled with water after the 1997–1998 and 2004 El Niño storm seasons and has a persistent high water table (when we first excavated in 2009 the water table was at ~0.5 m below the basin floor). The Grand Fire in May 2013 burned the surrounding slopes and subsequent mudflows deposited about 70 cm of sand and gravel across the Qyf surfaces and the western half of the basin (Figure S2).

Since 2005, we excavated more than 30 trenches across the site (Figure 2a); about half were vertical-walled trenches, ~1.5 m deep and ~1 m wide, and were oriented both fault-perpendicular to reveal faulting and fault-parallel to connect stratigraphy and show longer-wavelength deformation across the basin. For stability, most of the deeper excavations were cut with sloped walls, principally in the area of T1, where progressively deeper and wider trenches were excavated in order to resolve faulting, thickness changes in units, and the 3-D structure of the basin (Figures 2b and 2c) [*K. M. Scharer et al.*, 2014, 2015]. Although most of the recent faulting is

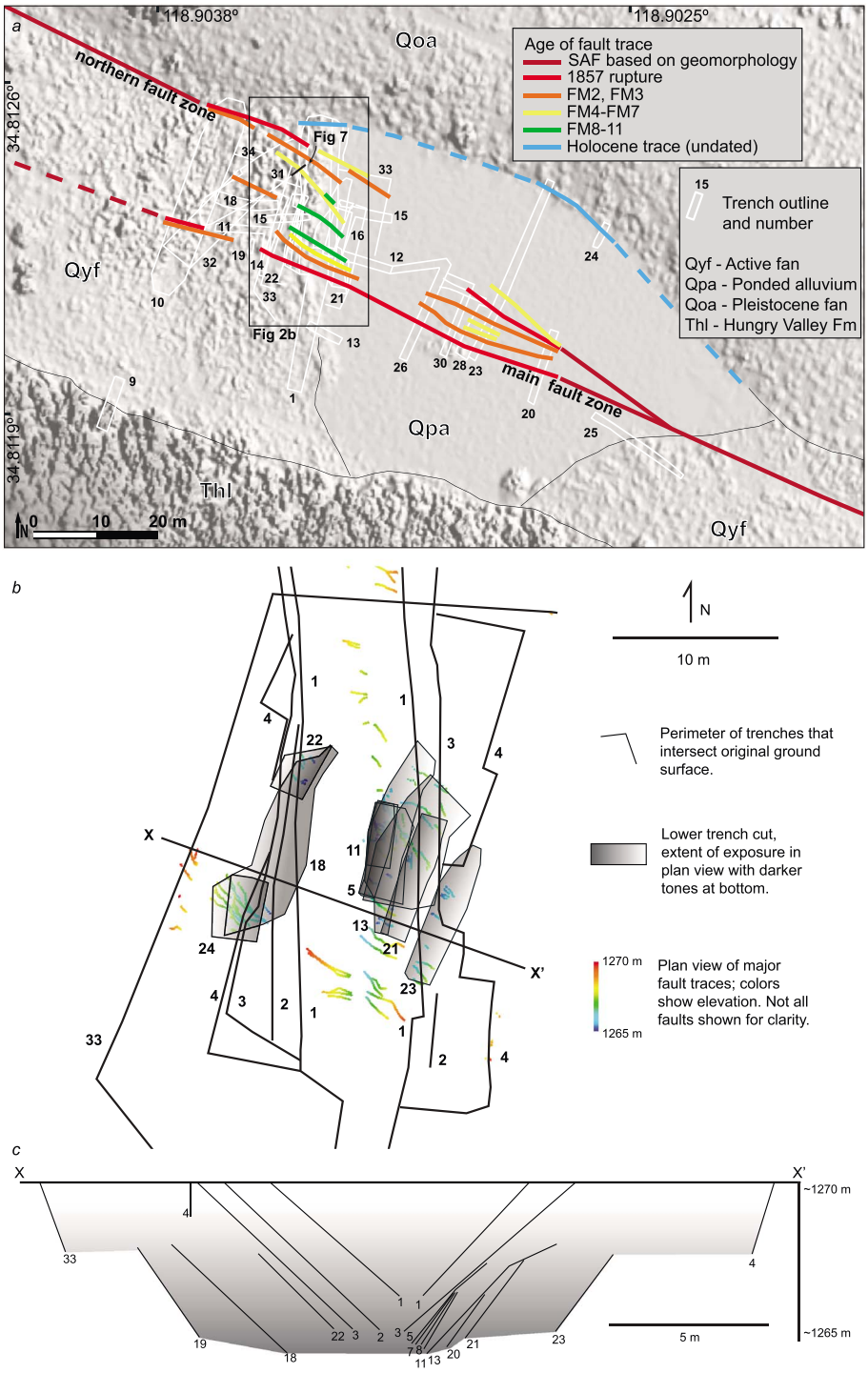

Figure 2. (a) Lidar hillshade model of the site including trench locations and general fault activity; lidar data from *Bevis et al.* [2005]. The colored lines show boundaries of major faulting associated with earthquakes FM1 through FM11 as discussed in text. Center of T1 is located at 34.812266°, −118.903344°. (b) Plan view of T1 cuts 1–33 and main fault traces observed in trench walls. (c) Cross section X-X′ shows relative location and elevation of T1 cuts with no vertical exaggeration. Line drawings of the trench logs are provided in Figure S1, and complete photomosaics are publically available in *Scharer et al.* [2014, 2015].

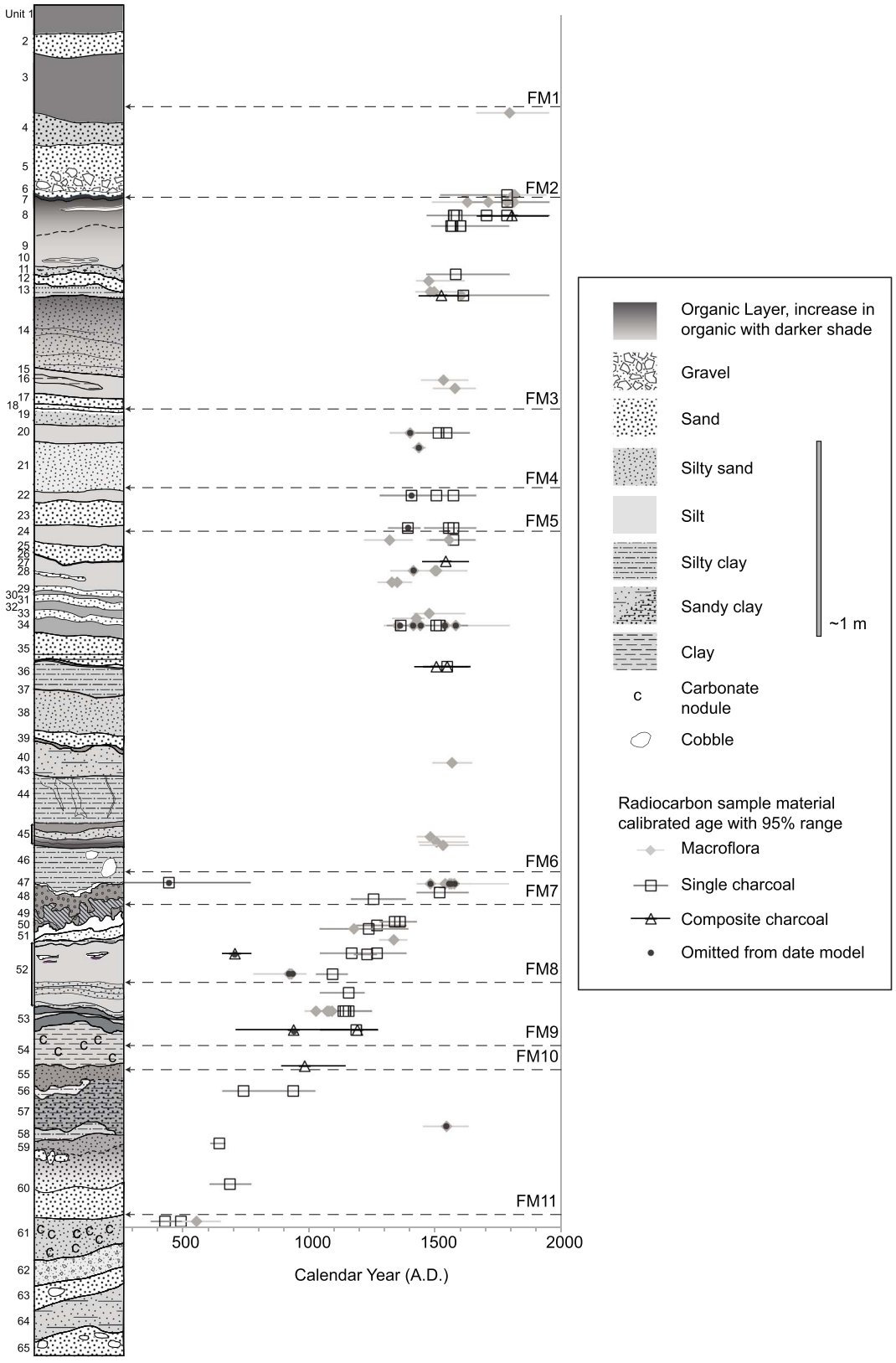

Figure 3. Composite stratigraphic column, radiocarbon dates, and earthquake event horizons.

restricted to the main and northern fault zones, excavations around the perimeter of the site show that the basin is in part structurally controlled (Figure 2a). Trenches T23 and T24 cross the north-central basin margin and exposed older colluvium and minor alluvial units that buttress against the northern scarp. Faulting in these trenches was minor and discontinuous and did not extend into the upper meter of colluvial deposits. Stratigraphic correlation from T1 to T23 and T24 establishes that the northeastern scarp has not been active in the last ~1000 years [*Zachariasen and Dawson*, 2012]. Similarly, in T9 on the southern margin, basin deposits onlap a landslide deposit of Pliocene Hungry Valley Formation and show no evidence of recent faulting. A charcoal radiocarbon sample from the base of this trench dates to 2758–2183 calendar B.P., indicating that the southern margin has not been deformed in the last couple of thousand years. In contrast, trenches in the northwest corner of the basin show more recent activity. In T10, for example, recent faulting juxtaposes younger fluvial and basin-fill deposits against older colluvium and Qoa terrace material. Trenches southwest of the main fault zone [e.g., the southern half of T1 (Figure S1), T9, T13, T25, and T26] revealed flat undeformed layers that provide further evidence that recent faulting has been focused along the main and northern fault zone.

The extensive network of trenches around the main and northern fault zone revealed two fault-controlled subbasins. The western subbasin is 30 m wide and at least 40 m long and shows progressive deformation on the main fault zone and a series of other strands to the north (Figures 2 and S1). A smaller more symmetrical basin, approximately 10 m wide by 40 m long, is located in the center of the site (T26, T30, T28, T23, and T20). Trench logs from the eastern subbasin are provided in *Weldon et al.* [2013] and *Zachariasen and Dawson* [2012]. Sedimentation rates are lower at this more distal setting, although some of the units were traceable in T12 across the relatively undeformed section between the subbasins.

We focused most of our efforts in the western subbasin because (1) the units are thicker at this more fan-proximal setting, (2) faulting patterns produced less over-printing, and (3) the lower stratigraphic package has more layers and distinct bedding contacts. Structurally, the western subbasin is formed by a series of en echelon and discontinuous faults that trend more northerly than the main trace and appear to connect the main and northern fault zones, resulting in a pull-apart geometry. By mapping the activity of discrete faults in the trenches, we show that the pull-apart grew deeper and wider with successive earthquakes through both distributed folding and discrete faulting of the ground surface (Figure 2).

2.1. Stratigraphy

The basin stratigraphy consists of alternating sequences of clayey-silt, silt, and sandy-silt deposits interbedded with organic-rich silt, sand, and gravel deposits. The composite stratigraphic column (Figure 3) shows the sequence of the upper 5 m of deposits in T1. In general, the stratigraphy alternates between finer grained, wetter conditions and drier, more bioturbated conditions at the site. From oldest to youngest the deposits include a lower sequence dominated by relatively clean sand with cobble layers and postdepositional carbonate nodules (units 65–55) that is overlain by a sequence of finer silt and organic-rich deposits (units 54–52). The middle part is dominated by well-bedded silt, clay, and sand sequences (units 51–47). Above the well-bedded units the deposits are mostly silt that is bioturbated and interlayered with a few continuous sand layers (units 46–8). The upper sequence consists of coarse sand and gravel layers (units 7–2), which are capped by the modern soil.

The wide variety of deposits reflects a mix of the material in the uphill sources of Precambrian gneiss and Hungry Valley Formation (Figure 1b). Based on clast lithology, the coarse sand and gravel deposits are sourced from both formations. Following the 2013 Grand Fire, a series of storms deposited sheets of clean sand interbedded with charcoal and organic material into the basin (Figure S2). This modern record provides evidence that the clean sand layers in the stratigraphy are the product of significant storm events (and if the clastic layers overlie charcoal-rich horizons, are likely postfire). In contrast, a few of the units (i.e., 47 and 51) are composed of laminated clean white silt and likely come from small outcrops of the lacustrine beds in the Hungry Valley Formation that are just upstream of the site. Layers that are predominantly silt are often strongly bioturbated and are thus interpreted to be the product of smaller storm events, aeolian contributions, and reflect slower, less episodic sediment accumulation in the basin.

2.2. Site Structure

Due to the extent of the trench network, we are able to document the progressive deformation and growth of the western subbasin over time and consider how the geometries of the deposits and the structures affect the appearance of surface deformation during each earthquake. There are two factors that are relevant in the

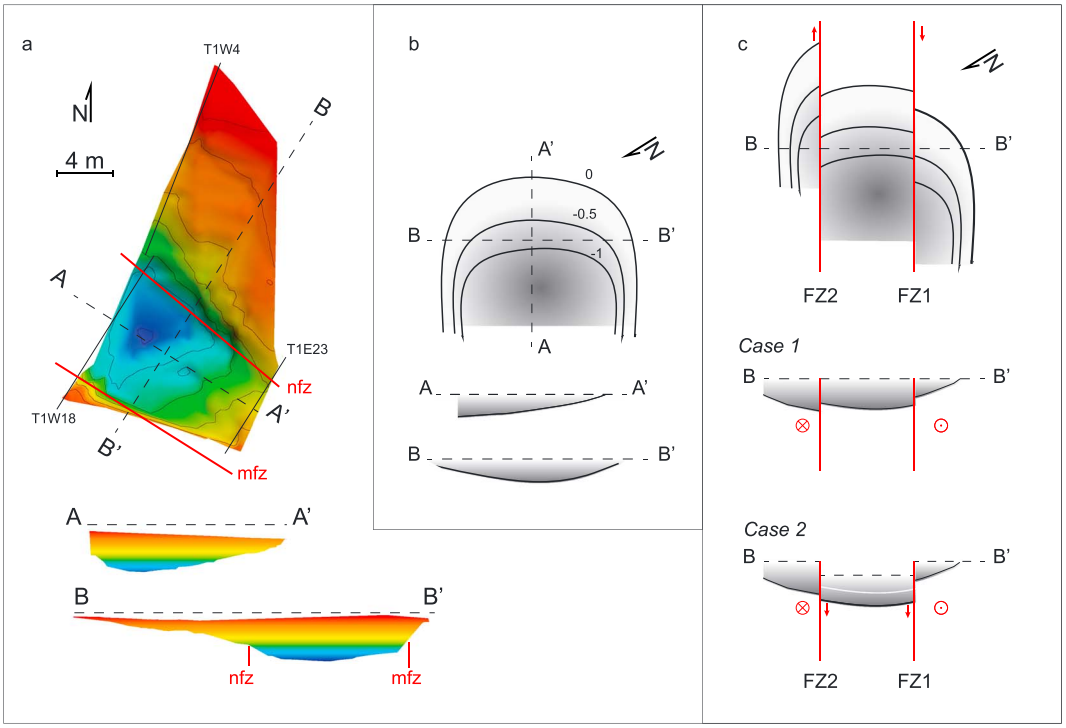

Figure 4. (a) Isopach map of unit 53 with 0.5 m contours from surveyed exposures in T1 (select perimeter trench locations shown in black). This surface shows cumulative evolution of the western subbasin since ~800 A.D. (thickest where blue). Cross sections A-A′ and B-B′ shown with no vertical exaggeration illustrate how the deposits thin toward the southeast (toward A′) and the basin edge is steeper along main fault zone (mfz) than northern fault zone (nfz). (b) Schematic of the unfaulted deposit with A-A′ axis parallel to fault zone (thickest in darker gray). Note the change in North orientation. The contours show elevation of the base of the deposit in meters relative to horizontal ground surface. The shape illustrated in the cross sections is a product of filling a structural basin formed during a previous earthquake. (c) Two fault zones cut through deposit with right-lateral offset. Effect is to place thicker section on north (left) side of fault against thinner section on south (right) side. Cross section B-B′, Case 1. If only strike-slip motion occurs, deposit will show apparent thickening to left (north) of each fault. Vertical motion (dip slip or folding) is not required to create the separation, and no depression is formed on the ground surface (dashed line). In Case 2, the pull-apart geometry produces dip-slip motion between the faults and structural lowering (the white line shows where deposit base is in Case 1). The elevation of deposit base in-between the faults will result from a combination of lateral slip and surface lowering in the basin. Note that apparent offset on FZ2 is opposite in motion compared to Case 1. Depression in surface between the faults will be filled by a subsequent deposit.

fault-perpendicular trenches (Figure 4). The first factor is the overall pattern of deposition at the site. In general, the entire package is thickest between the main and northern fault zones and thins to the southeast, away from the Qyf source fan. The units also taper on the northern and southern sides of the basin, most sharply at the main fault zone and more gradually across the northeastern half of the basin and the northern fault zone (Figure 4a). The modern surface gradient at T1 is less than 1°, so the deposit geometry can be simplified as a wide, elongate wedge with a west dipping base and a nearly horizontal upper surface. This wedge shape is a direct effect of the second factor, the pull-apart structure, which causes basin subsidence during individual earthquakes between the main fault zone and the northern fault zone. The width of the pull-apart has increased over time, from about 10 m wide during FM10 through FM6 to about 30 m wide by FM2 (Figure 2). The thickest portion of each unit or set of units (i.e., the depocenter) is also temporally variable, reflecting slight changes in the activity of individual fault strands from earthquake to earthquake. The wedge exposed in the trenches tapers from a maximum of ~5 m thick in the northwest to ~2 m thick in the southeast, and it is composed of individual units, or sets of units deposited between earthquakes, that vary in thickness by at most ~50 cm.

Faulting of the wedge-shaped deposits produces complex patterns, such as vertical separations and differing layer thickness in the trench walls (Figure 4c). If only horizontal slip occurred on a set of right-lateral faults cutting parallel to the long axis of the wedge, then the slip would produce apparent thickening on the

Table 1. Description of Event Indicators and Associated Quality Ranking

Quality	Description
0	Fault tip where upper termination not distinct due to unclear stratigraphy
1	Fault with minor offset. Minor and gradual thickness changes that could simply reflect depositional gradients rather than filling of earthquake-produced depression
2	Fault with moderate offset. Folding amplitude small, and thickness change above horizon of folding is moderate
3	Fault tip with distinct upward termination, moderate offset. Folding and thickness changes in layers above folding horizon that are substantial, but folding horizon has no clearly causative fault and (or) the horizon of folding is difficult to discern due to sedimentation rates
4	Fault tip associated with colluvial wedge or other layer thickness changes. Broad warping and large thickness changes in layer above folding horizon indicate rapid filling of depression, closely related to fault that moved to provide accommodation space
5	Fissures that are clearly filled with material that postdates inferred event horizon. Folding and growth strata in which it is clear that the topography was rapidly filled by a single sedimentation event and has a causal fault

north side of each fault relative to the south side, as a thicker portion of the wedge is translated laterally next to a thinner portion (Case 1, Figure 4c). However, with a pull-apart geometry, the separation of units across faults is a product of both the translation of the basal slope of the wedge and the amount of structural lowering in-between the faults (Case 2, Figure 4c). All of the T1 exposures reveal a pattern consistent with Case 2: the apparent separation across the main fault zone is down on the north, whereas it is down on the south across the northern fault zone. The consequence of this geometry is that the apparent lowering of the basin in each paleoearthquake is a maximum vertical displacement. Part of the separation is the result of the wedge shape inherited from deposition across an earlier, earthquake-produced basin, and the remainder is from surface lowering during the subsequent earthquake. For this reason we report the total surface lowering during each paleoearthquake by comparing the elevation of the (basal) paleoearthquake horizon inside and outside of the pull-apart basin, but do not use this to estimate the vertical slip component on the faults.

Although the overall pattern of faulting, deposition, and folding we have uncovered is consistent with a small right step producing transtensional deformation, some of the exposures show reverse separation (Figure S1). In many cases the separation in the exposure is a product of the slope of the trench wall and the dip of the fault; from 3-D trenching we can show that some faults that appear to be dipping in the sloped trench walls are actually subvertical. Other exposures with apparent reverse faulting are in fact steeply dipping, especially in the deeper exposures. Similar faulting geometries are seen in analogue models of pull-apart basins at the early stages of development of negative flower structures and at inward curving fault tips produced by gravitational collapse on the basin-bounding faults [*Dooley and Schreurs*, 2012; *Wu et al.*, 2009].

3. Earthquake Horizons

The microtopography produced in historic ruptures on strike-slip faults includes a range of scarp morphologies, from small, discontinuous tears to large open cracks in the ground surface to folding that can be several meters wide or appear as narrow linear troughs on the surface. Such features have been recorded in great detail by postearthquake mapping with lidar and photography [e.g., *DeLong et al.*, 2015; *Gold et al.*, 2013; *Nissen et al.*, 2014] and are rich data for understanding trench exposures of prehistoric ruptures. Often, the deformation varies along strike and displays a combination of these features over fault zones that are just a few meters to tens or more meters wide. As a trench site is effectively a point measurement along a single rupture, the evidence of a ground-rupturing earthquake is dependent on both (a) the width and magnitude of surface deformation and (b) subsequent preservation of that deformation. To understand the variability and styles of sediment disruption, we use the system in *Scharer et al.* [2007], cataloguing the morphologic and sedimentological evidence of ground deformation and assigning a rank indicating the quality of the evidence on a scale of 0 to 5 (Table 1). The data set of event indicators at Frazier Mountain is based

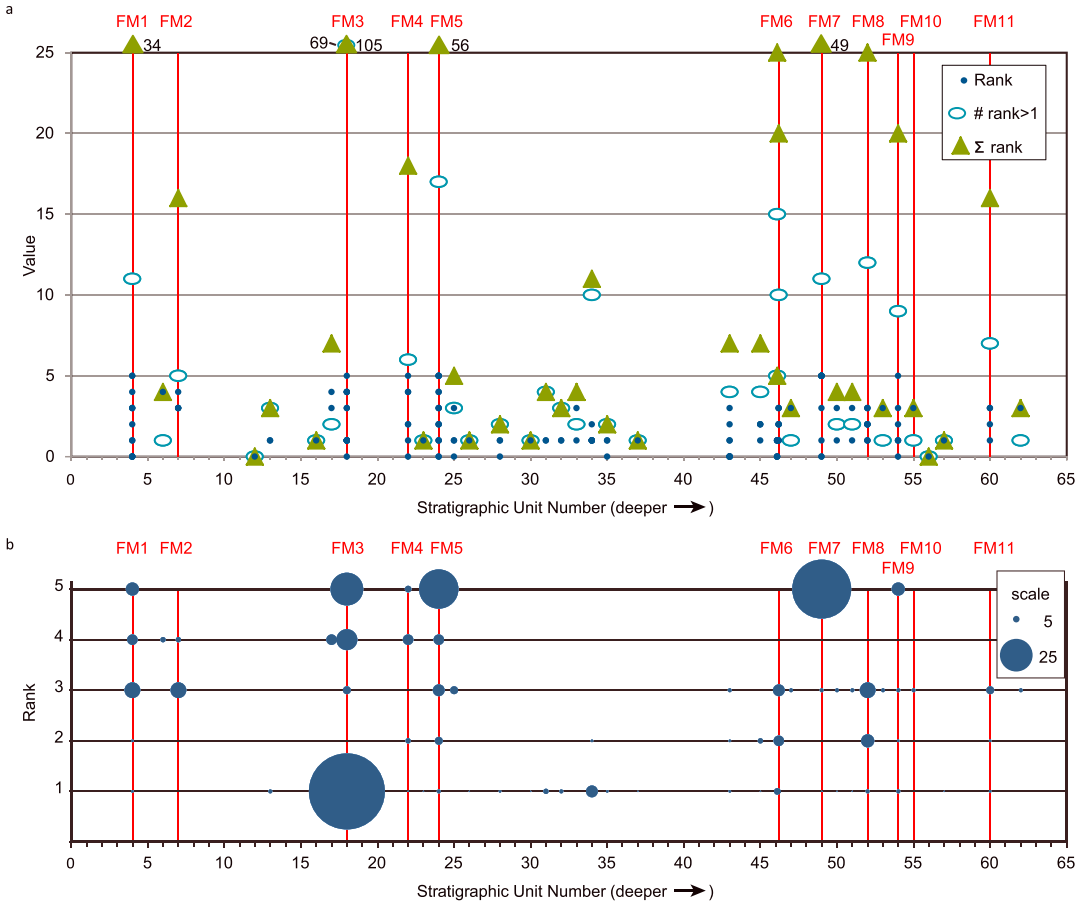

Figure 5. Combined plot of event indicator quality and number for all exposures of T1 based on ranking in Table 1 and catalogues in *K. M. Scharer et al.* [2014, 2015]. (a) Rank (1–5), the number of indicators with rank greater than 1, and the sum of the rank of indicators at all horizons. All of the qualified paleoearthquakes at Frazier Mountain (red lines) have at least one indicator with rank ≥3. Values greater than 25 are indicated at the top of the chart. (b) Alternate representation of the combined catalogue of event indicators to emphasize number of observations in each rank. The diameter of the symbol is scaled by the sum of the quality in each rank to illuminate the stratigraphic horizons with the largest number of high-quality indicators. For example, unit 4 has two indicators with a rank of 5, producing a symbol diameter of 10. Deformation at unit 18 (FM3) is unique as it includes a few high-quality indicators (5 indicators with rank 5) and many low-quality indicators (over 50 indicators with rank 1).

on the observations in a total of 22 cuts in T1, which are summarized in Figure 5 from the tables provided in *K. M. Scharer et al.* [2014, 2015].

We qualify the likelihood of an earthquake at each stratigraphic horizon based on consideration of the quality and the number of individual event indicators in each unit. Horizons with a sufficient number and quality of event indicators are considered as potential paleoearthquakes, and these are qualified as very unlikely, possible, probable, likely, or very likely. The paleoearthquake quality rating was applied based on the style and magnitude of deformation observed in the Frazier Mountain trenches, the depositional environment, and the number of observations (see *Scharer et al.* [2007] for additional discussion). Although there was no predefined criteria, units that qualified as paleoearthquakes scored highest in the sum of the rank of paleoearthquake events, number of observations with rank >1, and have at least one event indicator with rank ≥3 (Figure 5). Horizons qualified as probable (or better) paleoearthquakes are designated by with a "FM" prefix (e.g., FM1–FM11), and the age of each paleoearthquake is determined in the radiocarbon model.

In this section we evaluate the range of event quality, stratigraphic resolution, and morphology of deformation in each unit having at least one moderate quality observation (Figure 5) and discuss the likelihood that

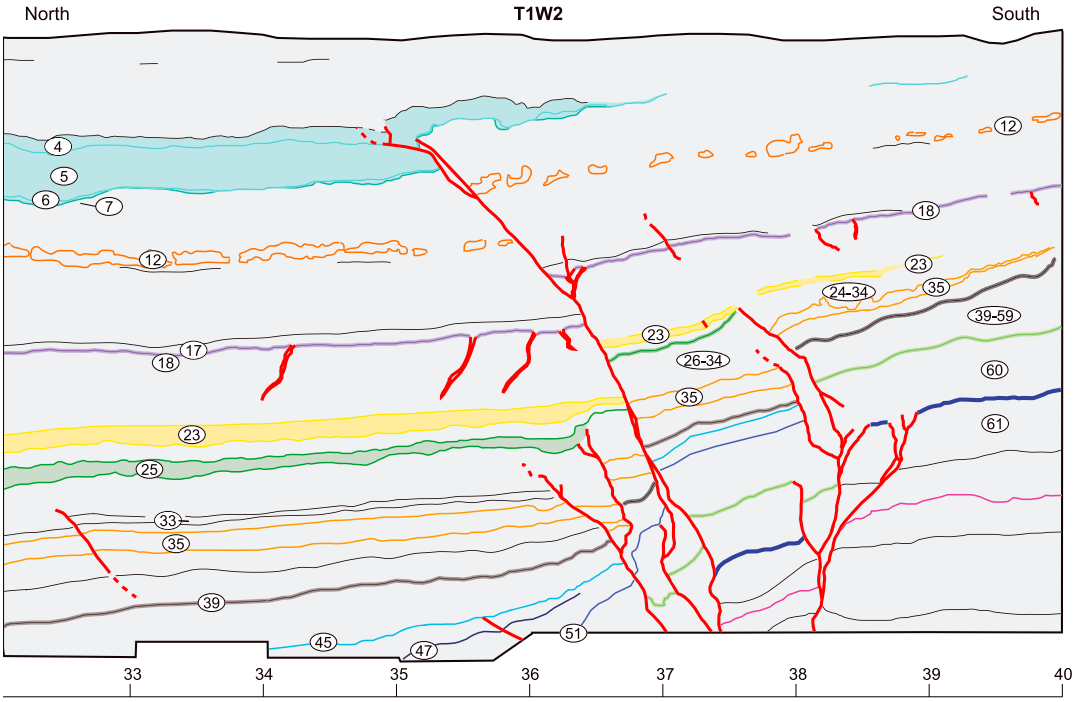

Figure 6. Eight meter section of T1W2 showing the main fault zone. Faults juxtapose an overall thinner section on the south side of the site against thicker section on the north side, reflecting both thinning of section along the basin margin and structural growth of the basin to the north (left) of the main fault zone. Units 51 through 39 also show shallowing dips to the north indicative of onlapping and growth strata. A fault zone in meter 38 branches out and terminates in two fissures at unit 61, providing evidence for FM11. The faulting pattern at meter 36 is typical for FM5, which is associated with discrete folding of unit 25 and subsequent burial by unit 24, indicating the earthquake occurred during the deposition of silt unit 24. At meter 38 the faulting that offsets unit 23 provides an example of low-quality event evidence associated with FM4 at this location, as the upper contact of unit 22 is not sharp at this location. FM2 is identified by the dramatic thickening of units 5 and 6 that filled a 30 m wide depression formed when unit 7 was at the ground surface. The rootless fissures associated with FM3 break unit 18 and are filled by unit 17. FM1 produces vertical separation of units 4 and older (the dip of the fault is apparent, a product of the sloping trench wall and fault oriented obliquely to the cut). See Figure S1 for trench location.

a ground-rupturing earthquake occurred when that unit was the ground surface. Units with a lower number and quality of event indicators are also considered for the potential of missed paleoearthquakes. Earthquakes FM1–FM5 were presented in detail in *K. Scharer et al.* [2014] so they are briefly summarized here; the focus is on the older events (FM6–FM11) and potential missed events. We also describe the timing of each paleoearthquake horizon with respect to dated layers and the depositional history at the site.

FM1 (Unit 4). *Very likely*. Deformation at the stratigraphic level of unit 4 includes faults with large vertical separation produced by lateral offset of units with variable thickness as well as broad folding that produced up to 70 cm of relief on the ground surface (Figure 6). This is the youngest paleoearthquake observed at the site and is interpreted to be the M_w7.7–7.9 historic 1857 earthquake based on its stratigraphic level and radiocarbon dating.

FM2 (Unit 7). *Very likely*. Event FM2 is designated as very likely due to the magnitude of folding which lowered the northwest portion of the site by as much as 80 cm when unit 7 was at the ground surface. Lateral thickness changes in organic-rich layer unit 7 suggests that the earthquake occurred early in the deposition of unit 7 and that surface lowering promoted additional accumulation of organic material before the site was inundated by sand and gravel (units 6 and 5, respectively).

FM3 (Unit 18). *Very likely*. Dozens of small fissures cut through unit 18 and are filled with sand from unit 17 (Figure 6). Because the majority of these fissures are not connected to faults with depth, we originally considered that this deformation could be the product of regional shaking from an earthquake elsewhere on the

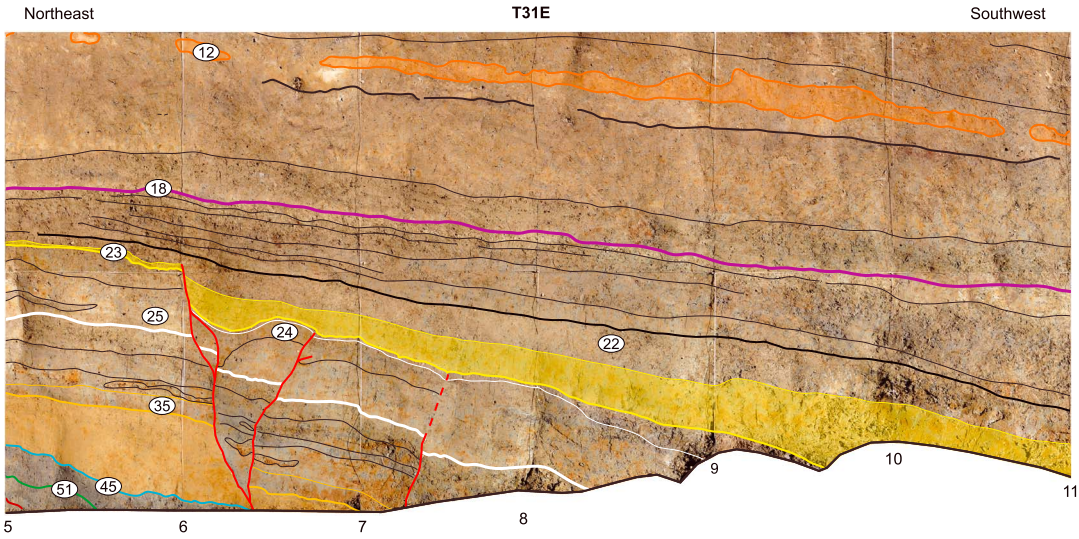

Figure 7. Faulting evidence for FM4 and FM5 in the north end of T31E. Faults offset the base of unit 22 in meter 6, providing evidence for FM4. Thickening of unit 23 across the exposure is likely the product of FM5. In other exposures this event is characterized by faults that terminate in clay unit 24 producing about 20 cm of vertical lowering of the ground surface which is subsequently infilled by unit 24 and finally capped by unit 23. Exposure location identified in Figure 2a.

SSAF or the Garlock Fault, or due to desiccation of the basin. Later excavations, however, revealed strong evidence of faulting at this horizon, indicating that the deformation is the product of motion on the SSAF. This includes several faults in T1 with ~10 cm of vertical separation that terminate in unit 18 and a fault in T32 that produced as much as 40 cm of vertical offset when unit 18 was at the ground surface [*K. Scharer et al.*, 2014]. Mapping the overall geometry of unit 18 shows that the western subbasin was lowered by 85 cm during this event through small offsets and distributed folding [*K. Scharer et al.*, 2014]. This earthquake was identified by *Lindvall et al.* [2002] as their event 2. The designation of very likely reflects the magnitude of surface lowering and quality of the faulting observed in T32.

FM4 (Unit 22). *Very likely*. There are five places where unit 23, a distinct, laterally continuous sand, is offset along faults with minor vertical separations and the faults terminate below the top of unit 22 (e.g., Figure 6). In order to investigate the minor faulting, at several locations we cut trench walls back and found that faults persistently terminated within unit 22 and thus are not likely to be subsidiary faulting from a younger event. The best evidence for an earthquake at this horizon is seen by a fault that offsets sand unit 23 but does not cut the top of unit 22 in T31E (Figure 7). Surface lowering indicated by the shape of the unit 22/23 contact in the western subbasin during this event is relatively small (~20 cm), so it is possible that this represents a moderate magnitude earthquake, the tail end of a larger rupture, or simply variability in slip along strike. As we observed multiple isolated locations where faulting at this horizon was not associated with evidence of subsequent earthquakes, we qualified the event as very likely despite the relatively low amount of surface lowering during the earthquake.

FM5 (Unit 24). *Very likely*. The highest-quality event indicators associated with FM5 are fault strands with vertical separation of up to ~1 m offsetting a distinct, laterally continuous sand (unit 25) and which terminate lower (early) in unit 24. In several exposures the clay unit 24 thickens across the fault scarp, suggesting continued in-filling across this event horizon (Figure 7). Sand unit 23 is uniform in thickness except where it crosses the scarps in unit 24, suggesting that the sand deposit could be the consequence of an individual storm deposit that filled the basin after FM5 but before FM4.

FM6 (Unit 46) *Likely*. The 20 event indicators in unit 46 are, in general, lower quality, mostly thickness changes ranked as 1 or 2, indicating that the amount of potential folding in the exposure is not significant enough to be uniquely associated with a discrete fold or fault scarp. There are, however, a few locations where the quality rank is 3, reflecting more significant (30%) decrease in unit thickness in T1 across the basin. The lower quality of the event indicators and general absence of discrete faulting evidence have made identification of a specific earthquake horizon difficult (Figure 8). Considering just the upper trench exposures in

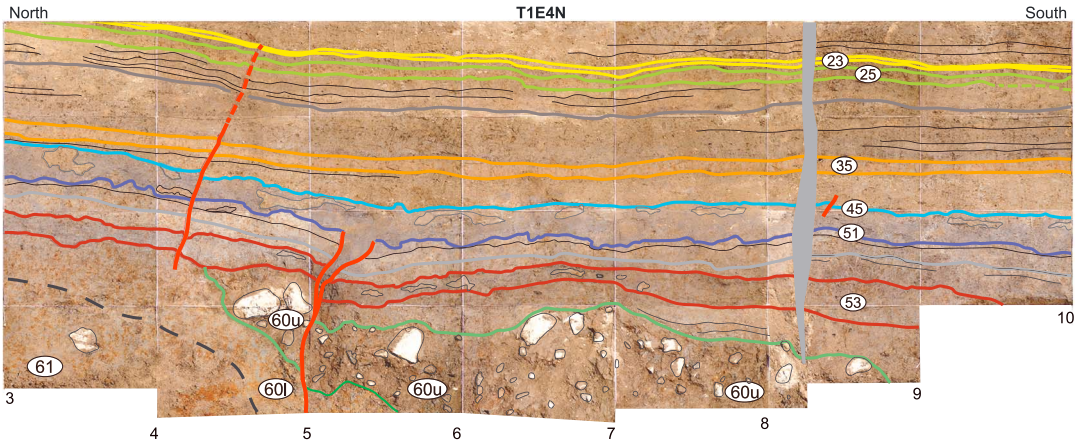

Figure 8. Portion of T1E4N illustrates challenges of recognizing discrete event evidence when stratigraphy is attenuated. Subtle thickness changes in units 45–35 could result from a folding event when unit 45 was at the ground surface or reflect continued filling after the fissure and faulting event in meter 5. The fissure occurred sometime after unit 51 was deposited, but due to massive character of units 45–50, it is not clear when the earthquake occurred in that interval at this location. This exposure does provide evidence of the oldest earthquake identified at the site (FM11), where the cobble gravel unit 60u onlaps the coarse sand units that are strongly folded below. See Figure S1 for trench location.

T1, *K. Scharer et al.* [2014] concluded that there was weak evidence for an event near the top of unit 46 (here identified as 46.1). This interpretation was based on the thickness changes observed in unit 44, assuming that the moderate deformation in unit 46 produced a depression that was progressively filled by units 46, 45, and 44. They further associated the thickness changes in the lower part of the unit (46.2) with continued filling of a depression formed by an earthquake that occurred when unit 49 was at the ground surface (FM7). *Scharer et al.* [2015] revised this interpretation based on the lower trench exposures in T1 that provide additional and higher-quality data on the locus and extent of the thickness changes in unit 46. Specifically, unit 48, a soil horizon, retains constant thickness across the lower exposures, suggesting that the ground surface was relatively flat when unit 48 was accumulating (Figure 9). The 30% increase in thickness of the overlying unit 46 would thus result from a fold scarp produced when unit 47 or the lower portion of unit 46 was at the ground surface. Further support for an event early in the deposition of unit 46 is indicated by blocks of unit 48 that were observed in unit 46, suggesting that unit 48 was disrupted and subsequently buried by unit 46 (rather than the thickness changes in 46 resulting from continued infilling from FM7 as originally interpreted by *K. M. Scharer et al.* [2014]). We observed no fault that can be specifically tied to the generation of a fold scarp when unit 47 was the ground surface. We thus infer that a fold scarp was produced by distributed deformation or by reactivation of the low-angle faults that are associated with FM7. In consideration of all of the exposures, and particularly the character of unit 48 in the lower trench exposures, we conclude that a paleoearthquake near the base of unit 46 is likely and that the deformation at 46.1 reflects continued infilling of a depression formed at 46.2, or possibly, a separate earthquake that had very limited surface deformation at the site. Filling of a synform produced during the deposition of unit 46 appears to continue through the deposition of unit 43; in combination units 43 through 47 fill a depression that produced 25 to 60 cm of surface lowering during this event.

FM7 (Unit 49) *Very likely*. There is strong evidence for an earthquake that deformed the ground surface during the deposition of unit 49, including faulting with reverse separation of the lower portion of unit 49 and older units, tight folding of these units, and distributed deformation of the unit 49/50 contact (Figures 9 and 10). Faulting and folding during this event are observed on both sides of a syncline that lowered the ground surface during this event by as much as 27 cm in T1E8. The fold increases in width over a span of roughly 10 m from a couple meters wide in the east (T1E21) to over 8 m wide in the west (T1W18). The FM7 paleoearthquake occurred during the deposition of unit 49, which locally pinches out on the fault scarp produced during faulting that affected the base of 49 and older units.

FM8 (Unit 52) *Likely*. The evidence for a ground-deforming earthquake early in the deposition of unit 52 comes from 2-to-3-fold thickness changes in unit 52 in most trench exposures and locally, preservation of interbedded sand and silt layers in the upper half of unit 52 that thicken toward the center of the fold and

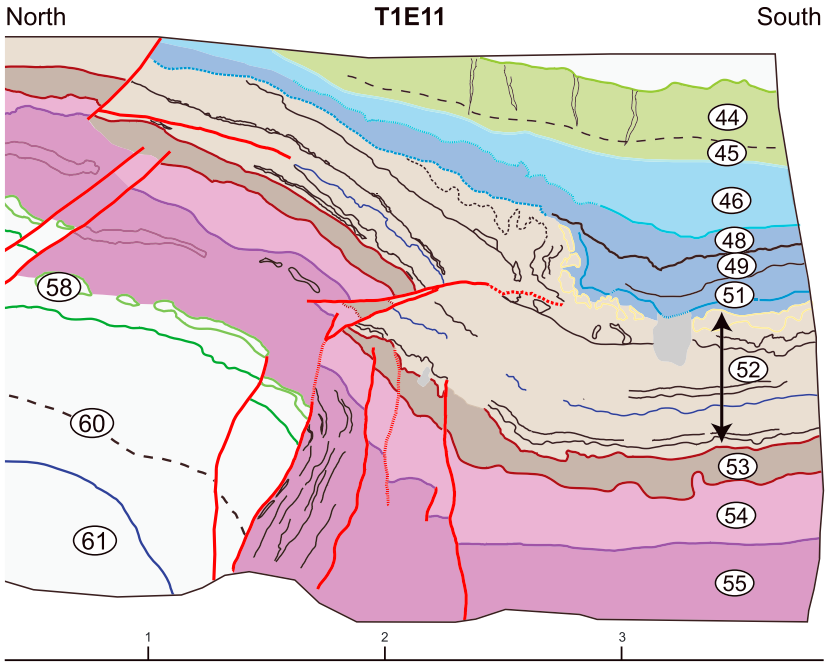

Figure 9. (T1E11). This section of T1E11 shows evidence for FM6 though FM10. The oldest evidence, associated with FM10, is the shear fabric developed in the fault zone between meters 1 and 2, here shown as subvertical thin black lines. The shear fabric becomes parallel to the unit 54/55 contact and does not extend into unit 54, indicating that unit 54 was not affected by that deformation and providing evidence for an event late in the deposition of unit 55. In this exposure, the evidence for an event at unit 54 (FM9) is limited to the thickness changes revealed by later faulting that juxtapose thinner portions of unit 54 to the north; note that unit 53 shows only slight thinning across the same span. In contrast, unit 52 is twice as thick within the syncline as on the edges; discontinuous subunits in the upper portion of unit 52 suggest that the thickness changes are the product of an earthquake (FM8) that produced a trough on the surface midway through the deposition of unit 52 and that may have produced the vertical faults centered at meter 2. Higher faulting clearly offsets unit 52 and folds units 51–49 providing strong evidence for an earthquake at unit 49 (FM7). At this location, unit 48 appears to have constant thickness across the fold scarp, suggesting that the southward thickening of unit 46 is the product of an earthquake during the deposition of this unit 46 (FM6). Faults like the low-angle fault in the upper left are observed in several of the lower exposures; they cut faults active during FM5 indicating that the low-angle faulting is fairly recent. See Figure S1 for trench location.

may represent growth strata (e.g., T1E3 meters 27–30 in *K. M. Scharer et al.* [2014]). Relief generated at the 52/53 contact is smallest in the eastern end of the site (17 cm in T1E23) but increases to the west as illustrated in Figure 10, and reaches a maximum of 48 cm in the westernmost exposure T1W24 [*Scharer et al.*, 2015], suggesting a synform that plunges to the west. Discrete faulting for this event is less clear largely due to overprinting; most of the faults that terminate in unit 53 or the base of 52 are co-located with later faulting and could thus represent splays from the event at unit 49 or later (e.g., Figure 10). The highest-quality faulting associated with an event during the deposition of unit 52 is in T1E11 (Figure 9) and is ranked as 3. In places where the subunits in unit 52 are not bioturbated, the lower portion of unit 52 is roughly parallel to unit 53, and subunits in the middle of 52 take up the thickness changes. The highest ranked indicator associated with unit 52 is a 3, but the excavations in the lower section were both fewer in number and more geographically restricted, so we qualify the paleoearthquake that occurred roughly midway in the deposition of unit 52 as likely.

FM9. (Unit 54) *Very Likely*. The best evidence for an earthquake during the deposition of unit 54 comes from T1E23 (Figure 11), where discrete faulting forms a 1–2 m wide graben in which a mix of material from unit 55 and 54 was deposited and subsequently capped by unit 53. The relief generated on the base of unit 54 during folding is 27 cm. In other exposures, evidence for an earthquake during the deposition of unit 54 comes from lateral slip causing juxtaposition of different thicknesses of unit 54. In many cases the faulting does extend higher (e.g., T1E11; Figure 9), indicating that some of the thickness changes could come from lateral slip during events younger than one at unit 54, but this cannot account for all of the lateral variation in the thickness

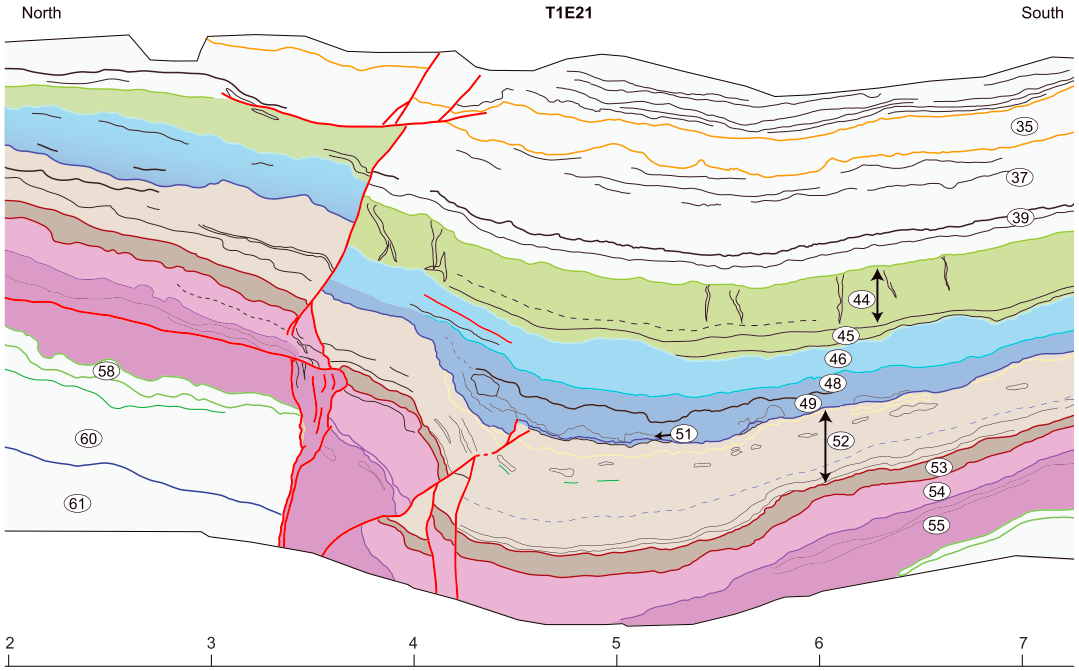

Figure 10. (T1E21). Faulting in this exposure is complicated by overprinting that illustrates thickness changes that are the product of folding associated with the pull-apart fault geometry (Figure 4). The oldest earthquake expressed here is seen in the twofold increase in the thickness of unit 54 from the base of the syncline (where it is unseen below the bottom of the exposure) through the southern half of the exposure. Shear fabric in the fault zone in meter 3 expressed as subvertical lines is truncated by faults that extend to the top of this exposure and low-angle faulting that occurred after FM5. As in T1E11, however, the shear fabric is restricted to unit 55, so the deformation must have been developed in an event late in the deposition of unit 55 or early in the deposition of unit 54 (FM10). Moving up section, faults that offset the base of unit 49 (FM7) juxtapose a section of unit 52 to the south that is twice as thick as 52 to the north of the fault, yet underlying unit 53 has constant thickness across the fault. This relationship reveals lateral thickness changes in unit 52 which are interpreted to be the product of deposition across a small depression caused by an earthquake after the basal subunits of 52 were deposited (FM8). See Figure S1 for trench location.

of unit 54 across this fault zone. We consider it very likely that an earthquake occurred early or midway through the deposition of unit 54.

FM10. (Unit 55) *Probable*. The graben in T1E23 also preserves evidence for an event associated with unit 55, an organic-rich silt (Figure 11). At this location unit 55 is ~50 cm thick, whereas it is less than 10 cm thick outside of the graben. We interpret this as evidence that a narrow sag pond formed during the deposition of unit 55, causing increased organic material to be preserved within the graben. The second line of evidence for this event is a vertical shear fabric present in narrow, fault-bounded slivers in unit 55 and older (Figure 9). The shears are subvertical but roll over and become parallel to the subhorizontal 55/54 contact, which suggests that faulting and shearing of unit 55 ended before unit 54 was deposited. Similar shear fabric in T1E21 (Figure 10) is truncated by later faulting and not as clear. Due to the spatially limited expression of this event we interpret that an earthquake during the deposition of unit 55 is probable.

FM11 (Unit 61) *Likely*. The event indicators we have documented associated with FM11 are present in the sandy units exposed on the margins of the western subbasin. There are two faults that splay out of the main fault zone and open into fissures at the base of unit 60 (Figure 6); despite their size and morphology, these fissures received a rank of 3 due to concerns about overprinting and the massive character of units above 60 that may obscure the upward continuation of these faults. On the northern side of the basin, dramatic evidence of folding and onlap is expressed where unit 61 is folded to subvertical and unit 60u, a matrix-supported cobble unit local to the northern side of the basin, thins across the fold (Figure 7). Due to lateral variation in the thickness of units 61 and 60 we are unable to determine if the folding adjacent to the northern fault zone (Figure 7) occurred at exactly the same time as the fissures formed on the main fault zone (Figure 6), but both types of features appear to occur just before deposition of unit 60. We conclude that at least one earthquake occurred during this time period and characterize it as likely.

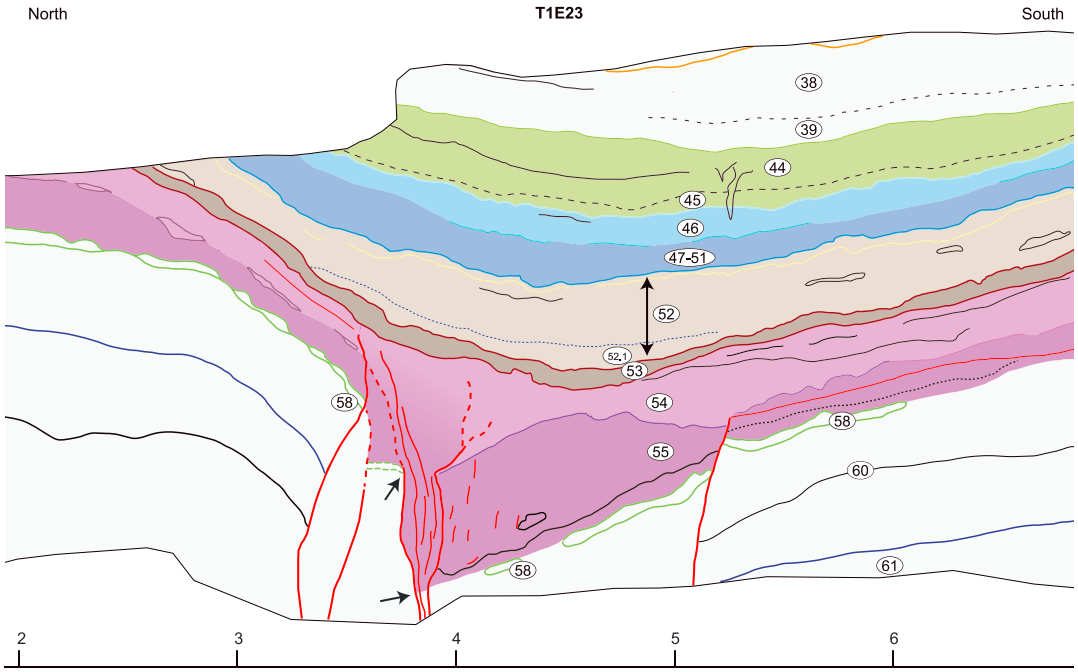

Figure 11. (T1E23). This is the easternmost deep exposure from the site. Here unit 55 shows dramatic thickness changes that we interpret to be the result of an earthquake (FM10). Within the fault zone unit 55 increases from its typical 15 cm thickness to over ~50 cm thick. Where thickest it is also much more organic and clay-rich, suggesting material that slowly deposited into an ~1.5 m wide sag pond formed during an event at unit 55. The vertical separation of unit 58 (highlighted with arrows) is similar to the total thickness changes of unit 55, reflecting accommodation space produced early in the deposition of unit 55 (FM10). Most of the faults in this exposure terminate within, or at the base of, unit 54 and thus provide clear evidence of a subsequent earthquake during the deposition of 54 (FM9). The northern fault zone is complex; several traces cut the base of unit 54 and cause apparent dip slip that places unit 55 (locally mixed with unit 54) on top of unit 54 (dashed faults that cross meter 4). Near meter 5, the 55/54 contact is offset by a subvertical fault that is connected to a low angle fault. Crosscutting relationships in other exposures suggest motion on the low-angle fault postdates deposition of unit 44; the relationship is not clear in T1E23. Dramatic thickness changes in unit 54, a massive silty clay, indicate deposition of unit 54 into the basin continued after the faulting during FM9 occurred. This exposure illustrates how the faulting patterns change rapidly along strike; the cut is only ~3 m from T1E21 (Figure 10), yet no evidence of discrete faulting during FM7 (unit 49) is present. See Figure S1 for trench location.

3.1. Unlikely and Missed Events

The paleoearthquakes identified as probable or better encompass the horizons for which we assigned an event indicator greater or equal to a rank of 3 (Figure 5). There are, however, a few intervals with lower quality evidence of ground deformation, a situation that typically occurs when the stratigraphic information on the exact event horizon is unclear. This can occur when faults have reduced slip up section (suggesting that the ground surface was not broken by the fault and the observed fault tip does not represent the event horizon), when faults terminate in an attenuated or subsequently bioturbated section (so the exact event horizon is unclear), or when minor variations in unit thickness is observed (a result of either minor tilting or folding of the ground surface or natural variation of unit thickness due to geomorphic setting). There are several intervals for which these types of low-quality indicators are observed which we do not interpret as evidence for a paleoearthquake.

3.1.1. Units 26–35

This stratigraphic interval is characterized by a series of alternating pale orange silty fine sand and grey silty clay layers that show no thickness variations along the axis of the basin; this interval is ~60 cm thick in both T1W18 and T1E3. Most (22 of 27) of the indicators in this interval are minor faults with small separation or reduction in slip up-section, which we interpret as accommodation faults associated with later folding and faulting events. The strongest evidence of growth strata is in T1W2 (Figure 6), which shows a 2.5-fold increase in the thickness of the section over about a 5 m span. While this thickness change would be considered moderate (Table 1), here it occurs across a series of faults that postdate this interval, and thus

likely reflect the lateral translation of thinner units on the southern margin of the site against thicker units within the basin. We note that the entire section is thin along the southern margin (i.e., units 1–60 are only 2 m thick), suggesting that the variation in thickness changes is a product of the wedge-shaped geometry of the basin rather than being related to fold-related thickening. For this reason we consider it unlikely that any of the low-quality event indicators are the product of a paleoearthquake between units 26 and 35.

3.1.2. Units 39–43

A similar issue is manifest in the indicators associated with unit 43, where fanning dips between units 43 and 39 in T1E3 [*K. M. Scharer et al.*, 2014] are possible evidence of growth strata. The amount of thickening is very minor, however, and could be the result of nontectonic thickness changes associated with thinning along the basin margin. There are four faults that are attributed to deformation in unit 43, but in all cases the stratigraphic position of the upward termination of faulting is not clear and the faulting could extend to higher levels. Unit 43 is also associated with a dozen cryptic sand-filled features that extend from the top of unit 43 down through unit 44. If these features are fissures, they are not the product of surface faulting at the site, as none are associated with offset of unit 43 nor are they connected to faults at depth. Consequently, the features could be the product of ground shaking from nearby earthquakes or may be roots or desiccation features unrelated to earthquake activity. For these reasons we do not identify any horizon between units 39 and 43 as a paleoearthquake.

3.1.3. Unit 45

The tally of event indicators (Figure 5) also includes variations in the thickness of unit 45 that are possible evidence of growth strata. Unfolding prominent horizons within this package, however, reveals that in T1E3, T1E4N, and T1E1, the difference in thickness changes was most significant across later faulting [*K. M. Scharer et al.*, 2014]. This indicates that the majority of the thickness changes are reasonably attributed to later offset of sedimentation patterns where the original deposit was thinner around the basin edge, as illustrated in Figure 4. T1E4 contains a good example of the uncertainty in using growth strata (Figure 8). In this case the tan silt units between unit 45 and unit 35 onlap onto a slight rise around meters 4–5. It is possible that this reflects an earthquake that occurred when unit 45 was at the ground surface. However, given the amount of deformation associated with events FM6 and FM7 (the fissure in meter 5 was probably produced during FM7; unit 49), we interpret that this location simply reflects continued filling into the basin from these older events. Further, there are no faults definitively associated with an event at this horizon. For these reasons we interpret that an earthquake at the elevation of unit 45 is unlikely.

3.1.4. Units 56–60

The number of event indicator observations decreases below about unit 56 (Figure 5), which is likely a consequence of the limited trench exposure of this lowest section relative to the numerous exposures (cuts) of the upper section. The small number of observations is also likely tied to the narrow zone of faulting during this time, which is only about 2–4 m wide during deposition of these older units. Only one trench cut (T1E23, Figure 11) exposed unit 58 and lower units across the entire pull-apart basin. Thus, it is possible that due to limited exposures, we have missed event indicators in units below about unit 56 and consider that the record may be incomplete below this layer.

4. Paleoearthquake Dating

4.1. Radiocarbon Dating

Layer ages are determined from 104 radiocarbon dates on a variety of organic materials (Figure 3 and Tables S1 and S2 in the supporting information). About half of the dates ($n = 47$) are on single pieces of charcoal selected from organic layers or found distributed in clastic layers. In some cases ($n = 9$) individual charcoal pieces were too small for a precise radiocarbon age, so we analyzed composites of multiple pieces of charcoal from the same layer. The remainder of the dates ($n = 48$) is on macroflora or bulk organic material, typically individual samples of partially decomposed stems, grasses, and reeds isolated from organic-rich layers. The layer and sample description and resultant radiocarbon age for each sample are presented in Table S2 and shown graphically in Figures 3 and 12. We note that where both types of material were dated in the same layer, the age of macroflora samples and charcoal samples often overlap and neither is generally older or younger than the other. We infer that similarity of charcoal and macroflora ages is due to deposition of short-lived shrubs and annual plants in the basin (in the winter the site is intermittently below freezing and

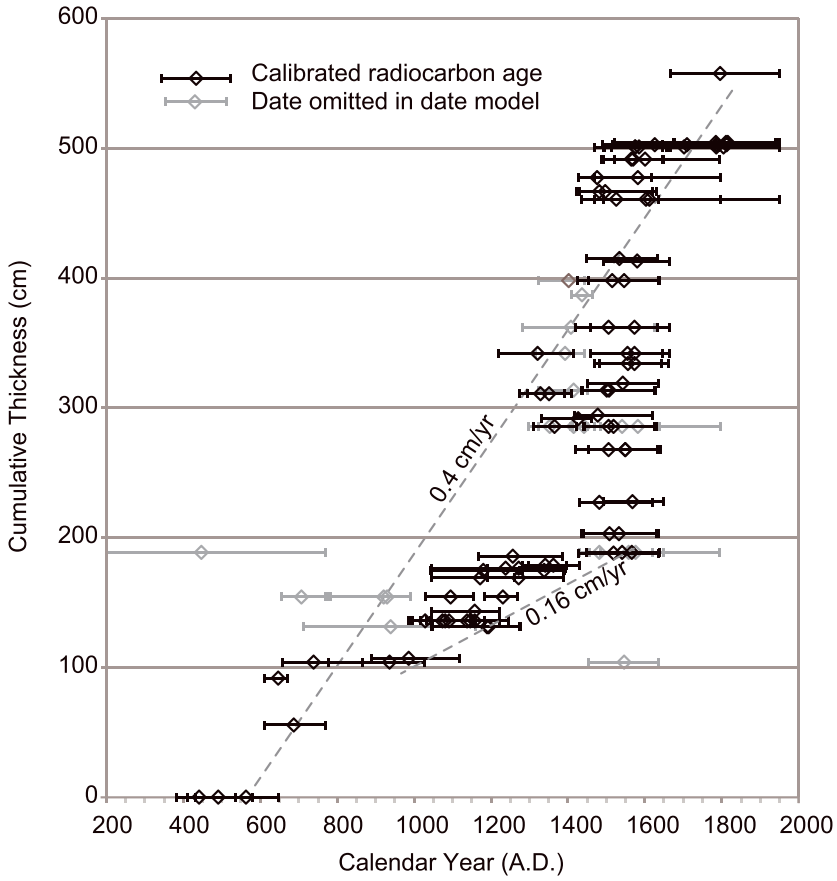

Figure 12. Plot of cumulative sediment thickness since unit 61 in T1 shows high sedimentation rate in the pull-apart basin, averaging 0.4 cm/yr since 500 A.D. Over 3 m of sediment accumulated between ~1450 and 1650 A.D. during the first half of the Little Ice Age [*Dingemans et al.*, 2014]. Table S2 provides reason that specific samples were omitted from date model.

receives snow). A short residence time of burnt material in the drainage is indicated by the narrow spread in charcoal ages for most layers (Figure 3).

4.2. Paleoearthquake Model Ages

We use a Bayesian approach to model posterior ages for the paleoearthquakes by using the Shaver code [*Biasi et al.*, 2002]. The final Shaver model for the Frazier Mountain site (Figure 13) includes 84 radiocarbon samples organized into 35 layers based on the type of material dated, the sedimentology of individual units, and consideration of the sedimentation rate (Figures 3 and 12 and Table S2). Layer ages are constructed from a set of sample dates from one or more units which are calibrated and joined into a probability distribution function (pdf). Modeled layers are identified with an "F" prefix, and if multiple samples from a single unit are combined in a layer, "j" is included as a suffix (e.g., F8j is the pdf for all of the samples from unit 8) (Figure 13 and Tables S1 and S2). Some thicker organic units were split into two layers to investigate the slower accumulation of these deposits (e.g., F7j are samples from the top of unit 7 and F7.5j includes samples from the lower half of unit 7). In constructing the Shaver model, 20 samples were not included (Table S2); about half were omitted as they were notably older than stratigraphically lower samples, indicating recycling of old plant material. The other half was omitted due to poor duplicate laboratory analyses. This problem was observed in a half-dozen samples that were sent directly from the field to the accelerator mass spectrometry laboratory. Unfortunately, the charcoal or macroflora were not isolated from matrix mud before analysis, so we suspect that a mix of matrix mud and charcoal or macrofloral material was analyzed and the poor duplicate results reflects changes in the amount of matrix mud that was included. To

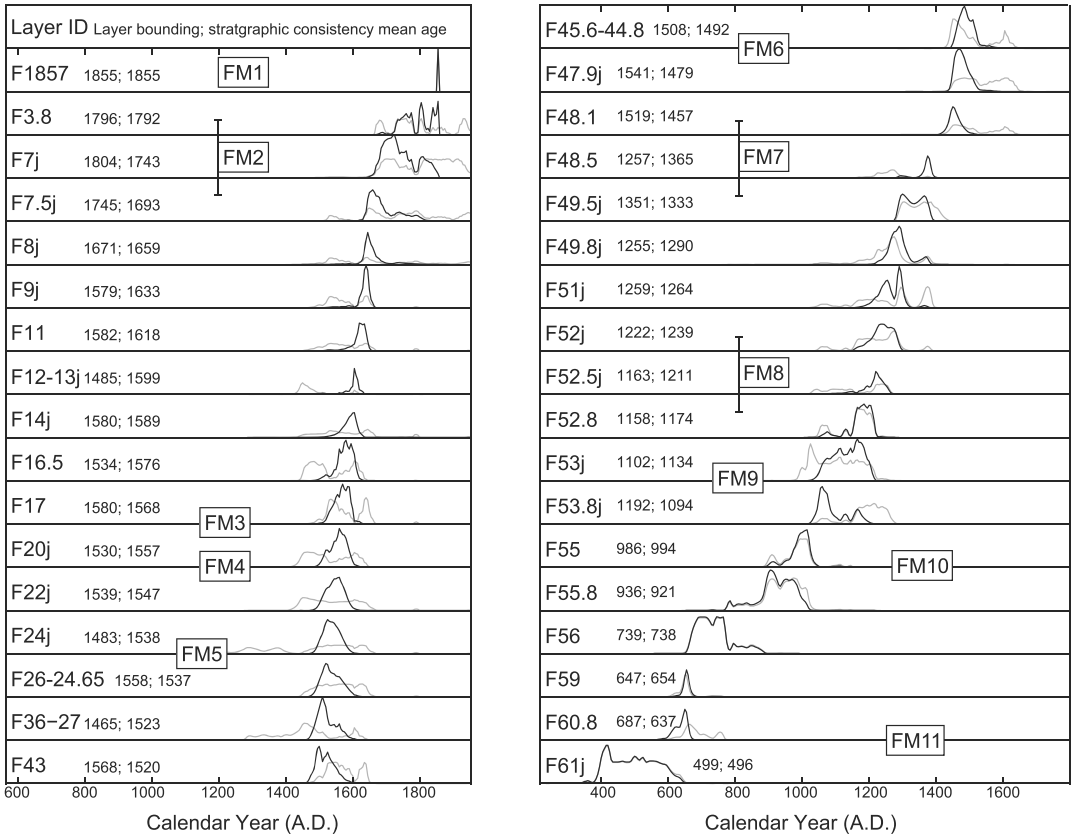

Figure 13. Shaver model of layer age pdfs. Prior distributions (light gray) are determined from calibration of laboratory 14C age to calendar years and when designated with a "j" the combination of multiple calibrated samples from a single layer. Posterior distributions (black) are determined by the application of Bayes theorem to the premise that the section should be stratigraphically consistent (i.e., stratigraphically lower layers are older than higher layers). Numbers after layer ID provide mean age for layer bounding (gray) and stratigraphic consistency (black) PDFs. The boxes indicate location of paleoearthquakes relative to dated layer; the vertical bars indicate when nonsequential ages were used due to uncertainty about event horizon relative to dated stratigraphic layer (e.g., folding associated with FM2 occurred some time between F7.5j and F3.8).

correct this problem, new macrofloral or charcoal material was isolated from the mud matrix and dated from each of the layers with poor laboratory reproducibility.

From the layer ages, Shaver uses Bayes Theorem to enforce stratigraphic consistency within a 12-layer sliding window that down-weights parts of the pdfs that are older or younger than stratigraphically lower or higher layers, respectively. The resulting stratigraphically consistent posterior layer ages typically fall within the peaks of the prior layer distributions (Figure 13). The sedimentation rate at Frazier is very high, exceeding 0.4 cm/yr in the center of the western subbasin (Figure 12). Over the last 1500 years, the fastest period of sedimentation occurred during deposition of layers 48 through 8, when ~3 m of material was deposited in about 200 years from ~1450 to 1650 A.D. (Figure 3). Typically, a fast sedimentation rate provides more precise ages of the layers (and thus the paleoearthquake ages). In this case, however, the fast sedimentation rate also occurs during a period of reversals in the radiocarbon calibration curve, resulting in calibrated (prior) layer ages with broad, double-humped uncertainties for layers F48.1 through unit F8j (Figure 13). The posterior ages for this 200 year long interval are affected by the large number of layers and their shape reflects the prior pdfs: posterior layer ages for F8j through F12–13j are forced into the younger peak in their prior pdfs, whereas the layers below are increasingly pushed into the older peak in their prior pdfs. While the resultant posterior layer ages are consistent with expectations (the base of the section is older than the top), it is important to recognize that the posterior pdfs are strongly controlled by the effect of the calibration curve on the sample ages.

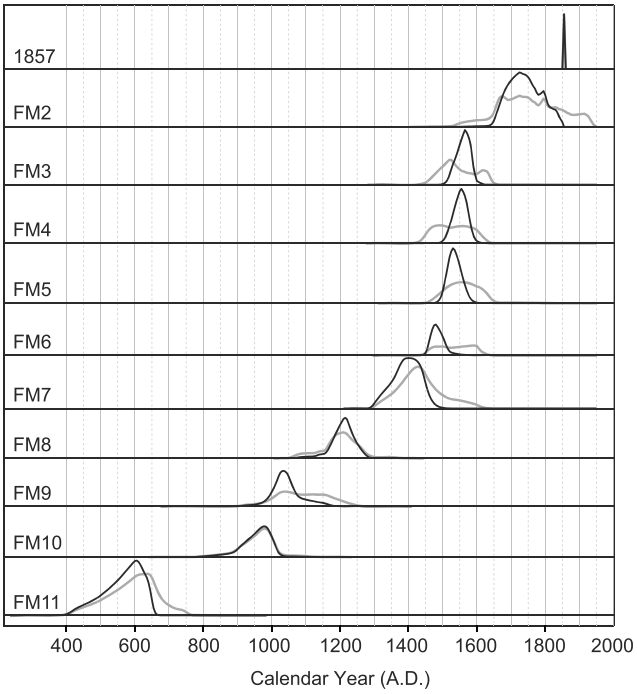

Figure 14. PDFs of earthquake ages for Frazier Mountain. The black lines show pdfs determined from stratigraphically consistent layer ages; the gray lines show pdfs using the untrimmed bounding layer ages.

Due to the high sedimentation rates at Frazier, we did not apply a sedimentation-rate constraint to the stratigraphically consistent posterior ages as previous studies have done at other Mojave section paleoseismic sites [e.g., *Scharer et al.*, 2007, 2011; *Biasi et al.*, 2002], as we felt that it would introduce artificially narrow layer pdfs. Nonetheless, there are significant steps in the layer ages of proximal units that are consistent with the sedimentation patterns. The oldest step is around ~1450 A.D., where ~90 years separate the mean ages of units F48.5 and F48.1. Unit 48 is a soil layer, and thus, this interval likely does reflect a stable, slow accumulation of material. The younger step is around 1690 A.D., where ~80 years separates the mean age of units F8j and F7j. Like the previous example, unit 8 is a soil horizon that likely records significant time, so we conclude that the steps in the ages do reflect changes in sedimentation patterns over time.

4.3. Earthquake Ages

The earthquake ages are determined from the ages of the bounding layers and thus typically have a 95% range of ~130 years (Figure 14 and Table 2). The large number of layers between units F48.1 and F8j have the effect of producing a series of relatively narrow age ranges of about 80 years for earthquakes FM6, FM5, FM4, and FM3. It is important to recognize that due to the sedimentation rate these narrow ranges may underestimate the epistemic uncertainty on the ages of these events, although the ages are reasonable given the amount and texture of material deposited between each paleoearthquake horizon. In contrast, due to reversals in the radiocarbon calibration curve over the most recent ~200 years which produce broad, multimodal pdfs, using radiocarbon dating alone, it remains unclear if the penultimate event at Frazier Mountain (FM2) represents the northern extent of a historically recorded 1812 earthquake.

5. Discussion

5.1. Range of Earthquake Magnitudes Recorded at Frazier Mountain

It is instructive to consider the historic record of moderate to large earthquakes on the Big Bend section of the SSAF to examine the range of earthquake magnitudes that produced ground deformation at the site. Historically, three *M*5.5–*M*5.9 earthquakes produced shaking in the region around Frazier Mountain [*Toppozada et al.*, 2002]. The best documented is the 1916 ~*M*5.6 earthquake which caused intensity VII damage and possible triggered slip on sections of the SSAF about 5–10 km west of the site [*Meltzner and Rockwell*, 2004; *Toppozada et al.*, 2002; *Branner*, 1917]. We find no evidence of small, recent slip at the site, indicating that either these sub-*M*6 events do not produce surface slip or the stratigraphy does not preserve events below about M6.

In contrast, FM1, which we infer from its stratigraphic position and radiocarbon dating to be the historic 1857 earthquake, produced significant deformation at the site, including over 0.7 m of surface lowering due to discrete faulting and folding of the ground surface (Figure 6) [*K. Scharer et al.*, 2014]. The closest measurements of lateral slip from geomorphic offsets are located 14 km NW and 20 km SE of the Frazier

Table 2. Paleoearthquake Ages From Shaver Model

EQ	Mean Age	95% Range		Paleoearthquake Quality
FM1	1857			Very likely
FM2	1735	1655	1830	Very likely
FM3	1560	1515	1595	Very likely
FM4	1550	1510	1585	Very likely
FM5	1530	1495	1575	Very likely
FM6	1480	1455	1535	Likely
FM7	1395	1310	1465	Very likely
FM8	1210	1120	1265	Likely
FM9	1035	960	1145	Very likely
FM10	960	840	1020	Probable
FM11	575	430	645	Likely

Mountain site [*Zielke et al.*, 2012; *Sieh*, 1978]. Based on the high or moderate to high-quality measurements from these locations, slip in 1857 had a lateral displacement of about 5 m through the Frazier Mountain site [*Zielke et al.*, 2012]. Combining this lateral slip with the 0.7 m of surface lowering documented in the pull-apart basin during 1857 results in a lateral to vertical displacement ratio of about 7:1 in the western subbasin for this earthquake. If this 7:1 displacement ratio is representative of surface lowering in the pull-apart during each of the paleoearthquakes and applied to the range of observed vertical deformation (0.2 to 1 m), horizontal displacements from the paleoearthquakes reported here range from 1.4 m to 7 m. Since the vertical displacements are maximum estimates (Figure 4), we infer that the minimum horizontal surface displacement recorded at Frazier Mountain is roughly 1 m. Based on empirical data of surficial slip in modern ruptures [*Biasi and Weldon*, 2006], this suggests a minimum magnitude estimate for each earthquake equivalent to M_w6.7 or greater.

5.2. Earthquake Recurrence

We calculate the interval length of time between individual paleoearthquakes by using the Shaver paleoearthquake model ages for the stratigraphically constrained event age pdfs (Figure 15). The longest mean interval (382 years) is between FM10 and FM11. Paleoearthquakes could be missing from this interval due to the restricted number of deep trench exposures and an incomplete section below about unit 56, as discussed above. For the record that we think is complete (since unit 56) the longest mean interval is 186 years. In contrast, a sequence of shorter than average recurrence occurs from FM6 to FM3, when the average interval is 28 years. This sequence of short intervals occurs during a period of rapid sedimentation that could reflect increased sediment flux to the site due to shaking and landsliding from these earthquakes (Figure 12). However, this period also overlaps with the Little Ice Age, a paleoenvironmental event seen globally and characterized by high run-off and increased moisture in Southern California and the American Southwest from about 1450 A.D. to 1850 A.D. [*Dingemans et al.*, 2014]. Thus, the pulse of rapid sedimentation at Frazier Mountain may be driven by increased sediment production in the catchment due to shaking and landsliding from the frequent paleoearthquakes and/or climatic forcing that increased sediment flux. It is possible that these factors lead to improved preservation of relatively smaller paleoearthquakes. FM4, for example, is associated with only ~20 cm of vertical deformation and could be an aftershock of FM5 that fortuitously was preserved due to the high sedimentation rate.

For the section that we recognize as complete (since unit 56), the average mean interval is ~99 years and the current elapsed period of 160 years is longer than 66% of the intervals. As a measure of recurrence variability, we estimate the coefficient of variation (COV) numerically as the standard deviation divided by the mean of the sample. To include paleoearthquake dating uncertainty, we sample many series from paleoearthquake age pdfs, which leads to a distribution of COV estimates. The COV provides a simple metric for estimating the variability among intervals; a COV of zero indicates perfectly periodic behavior, a COV equal to one is random, and values between these numbers are called quasiperiodic [*Goes and Ward*, 1994]. A COV greater than one reflects clustered behavior, with multimodal variability in interval length. The mean COV for the last 10 ground-rupturing earthquakes at Frazier is 0.7 (±0.1, 1σ) consistent with quasiperiodic behavior. If the section below unit 56 is considered to be complete and FM11 is included, the long interval between FM10 and FM11 causes an increase in the COV (to 0.9) that would indicate more random earthquake recurrence behavior.

The series of relatively short intervals from events FM6 to FM3 invites the question of whether the record can properly be considered to be "clustered" (Figure 15). The question is not easily resolved with the relatively short available event record; quasiperiodic processes can produce runs of short intervals by chance. Quantitatively, the case for clustering generally requires stronger differentiation and more prolonged

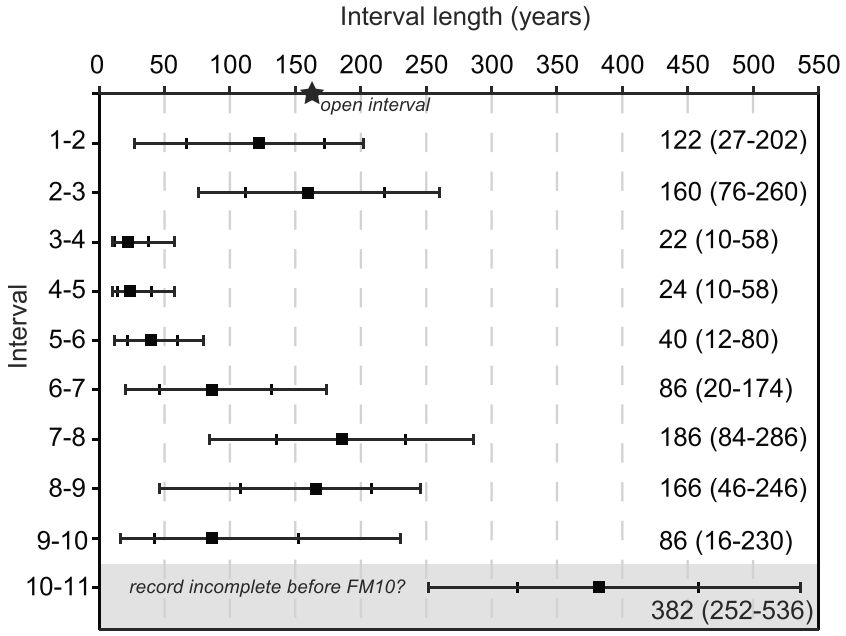

Figure 15. Plot of the interval length of successive paleoearthquakes determined in Shaver model (bars show 68% and 95% ranges on the length; mean and 95% range provided at right). Intervals are determined by sampling from the full paleoearthquake age pdfs. The star indicates elapsed time since last earthquake occurred in 1857. The longest interval is between FM10 and FM11, but limited exposures below unit 56 indicate that this may be an artifact of an incomplete record. From FM10 to FM1, <30% of the intervals are longer than the current elapsed time since the 1857 earthquake.

periods of shorter versus longer than average repeat times [*Goes and Ward*, 1994; *Biasi et al.*, 2002]. Many paleoseismic studies use "clustered" as a qualitative term to describe periods of shorter recurrence but do not provide statistical tests that distinguish their records from a random sample drawn from a Poisson distribution. Where COV estimates have been provided, a wide range of characteristics is reported, from clustered behavior on the Dead Sea Fault (COV = 1.0–1.7) to quasiperiodic behavior on the Alpine Fault (COV = 0.3) [*Berryman et al.*, 2012]. Sites on the strike-slip faults of the SSAF typically fall between this range, with COVs from 0.6 to 0.8 [e.g., *Dawson et al.*, 2008]. In the longest records, quasiperiodic COVs are found to be stable even when paleoearthquake quality, the possibility of missing earthquakes, and earthquake size are considered [*Scharer et al.*, 2010; *Rockwell et al.*, 2015]. Overall, earthquake recurrence patterns at Frazier Mountain is similar to the SSAF in general, and may reflect the high slip rate and relative isolation of this fault compared to more complex fault networks [e.g., *Berryman et al.*, 2012].

5.3. Correlation to Other Sites

We develop a potential rupture history for the Carrizo, Big Bend, and Mojave sections of the SSAF under the assumption that the same paleoearthquake spans proximal sites if their paleoearthquake ages overlap in time (Figure 16). In this way, the model is designed to identify the largest possible earthquakes in the record. An alternate, more probabilistic approach would be to develop candidate sets of possible ruptures derived from the paleoearthquake ages and slip data and infer ensemble magnitude and frequency properties from them [e.g., *Biasi and Weldon*, 2009]. Based on empirical relationships, ruptures that span the minimum 100 km from Frazier Mountain to each neighboring site would be equivalent to M_w7.3 earthquakes and ruptures that occurred at both adjacent paleoseismic sites north and south of Frazier Mountain would be 200 km long and equivalent to M_w7.5 or greater [*Wesnousky*, 2008]. This range of magnitudes is consistent with independent data on the surface displacement from geomorphic offsets that are ≤5 m per earthquake along the Carrizo, Big Bend, and Mojave sections [*Zielke et al.*, 2012].

The maximum rupture model (Figure 16) since 1300 A.D. is the same as discussed in *K. Scharer et al.* [2014]. In this model, a remaining uncertainty is the correlation of FM2 with other sites. *Toppozada et al.* [2002] considers the historic record for the SSAF at the latitude of Frazier Mountain site to be complete for $M \geq 6.5$ earthquakes since about 1800 and place the 8 December and 21 December, 1812 earthquakes on

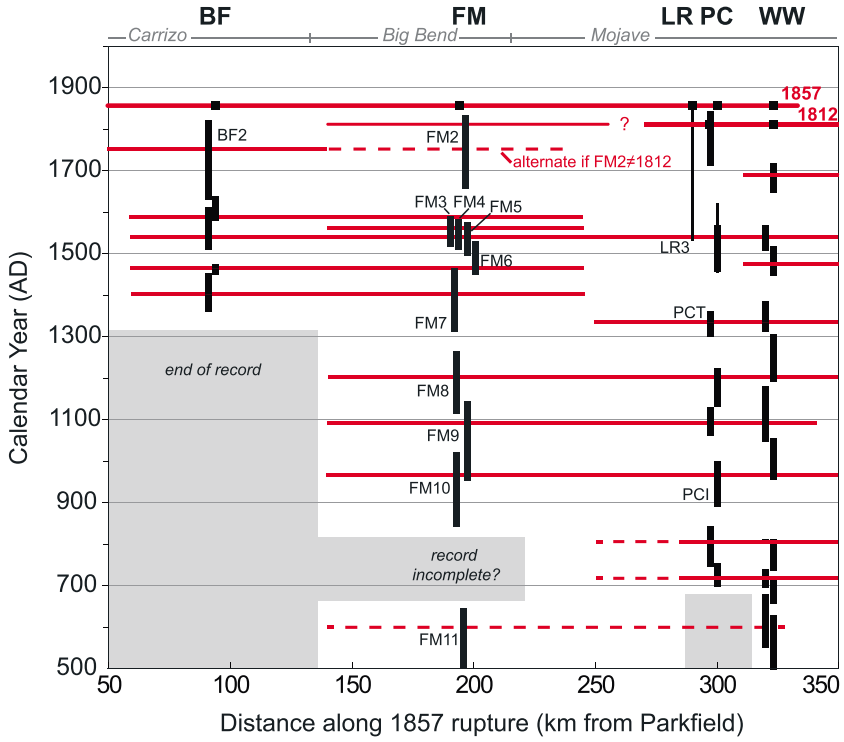

Figure 16. Correlation diagram showing potential rupture history of SAF earthquakes along the Carrizo, Big Bend, and Mojave sections of the SSAF (Figure 1) assuming that contemporaneous earthquakes at neighboring sites are the same earthquake. Many alternatives to this history are possible; this model determines the longest possible rupture given the chronologic data. The black vertical bars represent 95% range on individual earthquake ages from each site except for at Littlerock where three earthquakes are observed since 1525 A.D. (thin vertical line). The horizontal red lines show possible rupture extent of paleoearthquakes. For simplicity the ruptures end midway between neighboring sites. The pattern since 1300 A.D. is unchanged from *K. Scharer et al.* [2014] and shows that only one additional 1857-size earthquake is permitted. From 900 to 1300 A.D., the Big Bend and the Mojave sections have similar records, each with three earthquake Paleoearthquake ages from BF [*Akçiz et al.*, 2010], LR [*Pruitt et al.*, 2009], PC [*Scharer et al.*, 2011], and WW [*Weldon et al.*, 2004].

the SSAF. *Dolan and Rockwell* [2001] propose that the later earthquake occurred on the San Cayetano Fault. Radiocarbon dates and a pollen analysis of the upper section at Frazier Mountain site are unable to resolve this question. Although only the tail of the 95% range of FM2 (1655–1830 A.D.) is in the historic period, it could nonetheless be a historic event in 1812, so we place the northern terminus of FM2 at the location suggested by *Toppozada et al.* [2002]. Given the dating and historic uncertainties, we present alternate models in which FM2 is either (1) the northern extent of the historic 8 December 1812, (2) a separate historic event on 21 December 1812, or (3) correlates to BF2 and would likely precede the beginning of the historic record ("alternate" in Figure 16).

The maximum rupture model (Figure 16) includes one location where paleoearthquake ages overlap yet have not been correlated: the PCT and FM7 earthquakes around 1350 A.D. Here *K. Scharer et al.* [2014] argued that PCT and FM7 are unlikely to be contemporaneous based on the stratigraphic position of the paleoearthquake horizons relative to climatic changes preserved in the sedimentological record at both sites that reflect transition from the Mediaeval Warming Anomaly to the Little Ice Age. As a consequence, based on the paleoearthquake ages, only one other 1857-length rupture around 1550 A.D. is possible given the records at Bidart Fan, Littlerock, and Pallett Creek (Figure 16).

From ~800 A.D. to 1300 A.D., the Frazier Mountain record is quite similar to the Pallett Creek and Wrightwood records, each with three earthquakes (Figure 16). Due to overlap of ages at Frazier Mountain, we use proxy climate information provided by the sedimentological record at each site to inform the correlations. In this period, the most distinct interval in the Pallett Creek record is a thick organic section in which PCI occurs (891–1001 A.D. [*Scharer et al.*, 2011; *Sieh et al.*, 1989]). That section is similar to the organic-rich interval at

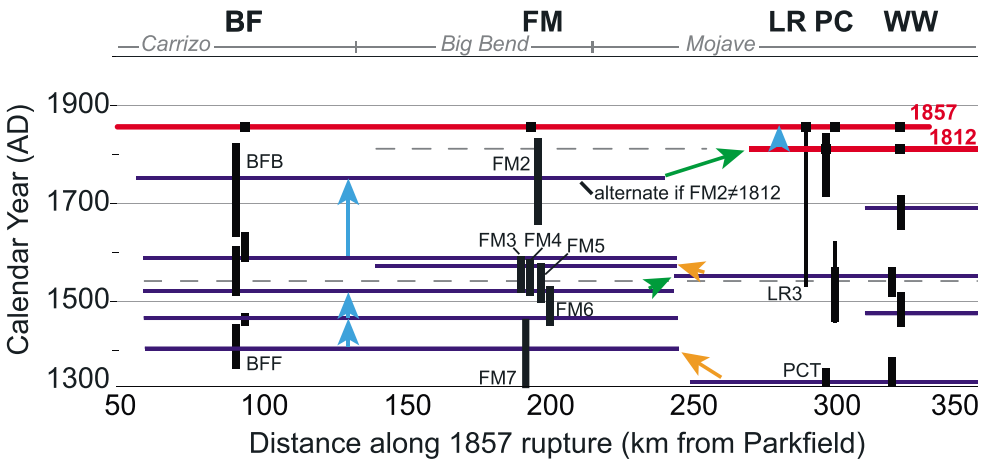

Figure 17. Examination of alternate rupture history since 1300 A.D. for directional patterns in earthquake sequences [e.g., *Perrin et al.*, 2016]. The red horizontal lines are historic ruptures, the dark blue horizontal lines are paleoearthquakes, and the dashed gray lines show ruptures that have been changed from the maximum model of Figure 16. Here we provide an example where neither 1812 earthquakes ruptured through Frazier Mountain. The green arrows show sequences that rupture to the southeast, the orange arrows show sequences that rupture to the northwest, and the blue arrows show ruptures that re-rupture the same location. Although each rupture connecting BF and FM could be split into separate events, we do not know a priori which event occurred first and thus cannot determine a cascade direction.

Frazier Mountain that accumulated during units 55–53 and which bound FM10 (Figure 3). In contrast, FM9 occurs after the thick soil of unit 53. Thus, although the dates of FM9 and PCI also overlap based on radiocarbon ages we correlate FM10 and PCI based on both the strong radiocarbon age overlap and the sedimentological observations. Unfortunately, there is no record of dated earthquakes before ~1300 A.D. northwest of Frazier Mountain, so we are unable to determine if these events are large, 1857-style earthquakes ($>M_w7.7$) or limited to the 150–200 km of the Big Bend and Mojave sections and thus equivalent to $M_w7.5$ or larger if they continue to the southeast. If the maximum rupture history is correct, it indicates that, at most, the Big Bend and Mojave sections rupture together roughly 50% of the time. For ruptures that did not break both of these fault sections, further paleoseismic studies between Frazier Mountain and Littlerock are needed to determine their rupture length and whether they terminated at persistent locations.

A spectrum of event sizes is possible in alternate rupture histories that respect geological observations. At one end, each prehistoric earthquake at Bidart Fan, Frazier Mountain, and Pallett Creek could be individual sub-100 km long events that did not rupture the proximal site, but this requires an unlikely case where to be large enough to cause ground rupture, each rupture must be roughly centered on the paleoseismic site. We consider it more likely that many of the paleoearthquakes do correlate and extend some distance along the fault. In the middle of the spectrum, the possible long rupture at ~1550 A.D. could be split into two or more ruptures, and some of the ruptures spanning Bidart Fan and Frazier Mountain could be separate. *Perrin et al.* [2016] propose that cascades of earthquakes propagate in the long-term direction of fault growth, illustrated, for example, by the historic sequence on the North Anatolian Fault. A model exploring this idea on the SSAF since 1300 A.D. does not support the hypothesis, as an equal number of ruptures cascade to the northwest as to the southeast, where these sequences can be determined within radiocarbon uncertainties (Figure 17). The Carrizo, Big Bend, and Mojave sections are mature, characterized by large amounts of total displacement (~300 km) and a high slip rate. Thus, the geometric segmentation found to be important in less mature, lower total slip faults [*Perrin et al.*, 2016] may not be as strong a control on rupture behavior for this part of the SSAF.

Regardless of the rupture model, we find that the dominant feature of the paleoearthquake record since 1300 A.D. is more frequent ground-rupturing earthquakes on the Carrizo and Big Bend sections than on the Mojave section. Such behavior is consistent with earthquake cycle modeling in which the misalignment of the Mojave section with North American-Pacific plate motion develops higher earthquake cycle static stresses [*Lin and Stein*, 2004] and less frequent ruptures in dynamic models [*Duan and Oglesby*, 2005]. The pattern could also reflect a reduction in slip rate on the SSAF toward the Mojave observed in

geodetic models [e.g., *Field et al.*, 2015]. Addition of paleoenvironmental data or slip data that allow us to test contemporaneity of paleoearthquakes at proximal sites is needed to lengthen the record and to examine the stability of this pattern.

6. Conclusion

The Frazier Mountain paleoseismic chronology is the longest record from the Big Bend section of the SSAF and is comparable in length to other sites on the Mojave section. For this reason it serves as an independent test on the recurrence behavior of the SSAF and provides new data that refine our knowledge of the rupture history along this fault. The average depositional rate of 0.4 cm/yr and the structural setting of the site, a small pull-apart basin that has grown in successive earthquakes over the last 1500 years, contribute to a robust paleoearthquake chronology marked by distinct earthquake horizons. Combination of the event indicator data from T1 [*K. M. Scharer et al.*, 2014, 2015] highlights 11 horizons that are identified as paleoearthquakes based on the sedimentological and geomorphic evidence at each horizon; FM1, FM2, FM3, FM4, FM5, FM7, and FM9 are qualified as very likely; FM6, FM8, and FM11 are qualified as likely; and FM 10 is qualified as probable. Due to the limited exposures of deposits in the fault zones below unit 56 we infer that the record may be incomplete prior to FM10, or about 800 A.D.

Paleoearthquake ages are calculated using a Shaver model [*Biasi et al.*, 2002] of 84 individual charcoal and plant remains grouped into 35 layers. Since circa 800 A.D., the earthquake chronology at Frazier Mountain shows similar temporal patterns to other sites along the southern SSAF such as Bidart Fan, Pallett Creek, and Wrightwood. The average interval between earthquakes at Frazier Mountain is ~100 years, and the individual interval means vary between 22 and 186 years. The mean COV for this chronology determined from the posterior pdfs of the earthquake ages from FM10 to FM1 (1857 A.D.) is 0.7, indicating quasiperiodic behavior. Most (66%) of the intervals are shorter than the current elapsed time (160 years) since the 1857 earthquake. Previous work established that correlation of paleoearthquakes along the Carrizo, Big Bend, and Mojave sections permitted that in the last ~700 years only one other rupture around 1550 A.D. could have been as long as the historic M_w7.7 earthquake in 1857 [*K. Scharer et al.*, 2014]. These new data extend the rupture history and explore the similarity between the Big Bend and Mojave sections of the SSAF. Both Frazier Mountain (Big Bend section) and Pallett Creek (Mojave section) have three earthquakes recorded between ~800 and 1300 A.D. If these represent individual earthquakes that spanned the 100 km between sites, then each has a minimum magnitude of about M_w 7.3 [*Wesnousky*, 2008]. The long record shows that ruptures span the Big Bend and Mojave sections at most 50% of the time, about once every biennial.

Acknowledgments

Funding for this work was provided by internal and external grants from the National Earthquake Hazard Reduction Program (05HQGR0071, 09AP00012, and 11AP201223), the National Science Foundation (0838294), and the Southern California Earthquake Center. SCEC is funded by NSF Cooperative Agreement EAR-1033462 and USGS Cooperative Agreement G12AC20038. The SCEC contribution for this paper is 7187. Data presented herein are available in the tables and references. We are thankful for reviews by Suzanne Hecker, Scott Bennett, and Olaf Zielke, Ramon Arrowsmith, and the Associate Editor. The work would not be possible without the assistance of numerous students from Appalachian State University, University of Oregon, and Pasadena City College.

References

Akçiz, S. O., L. G. Ludwig, J. R. Arrowsmith, and O. Zielke (2010), Century-long average time intervals between earthquake ruptures of the San Andreas fault in the Carrizo Plain, California, *Geology*, *38*(9), 787–790.

Berryman, K. R., U. A. Cochran, K. J. Clark, G. P. Biasi, R. M. Langridge, and P. Villamor (2012), Major earthquakes occur regularly on an isolated plate boundary fault, *Science*, *336*(6089), 1690–1693, doi:10.1126/science.1218959.

Bevis, M., et al. (2005), The B4 Project: Scanning the San Andreas and San Jacinto Fault zones, Abstract H34B-01 presented at 2005 Fall Meeting, AGU, San Francisco, Calif.

Biasi, G. P., and R. J. Weldon (2006), Estimating surface rupture length and magnitude of paleoearthquakes from point measurements of rupture displacement, *Bull. Seismol. Soc. Am.*, *96*, 1612–1623.

Biasi, G. P., and R. J. Weldon (2009), San Andreas Fault rupture scenarios from multiple paleoseismic records: Stringing pearls, *Bull. Seismol. Soc. Am.*, *99*(2A), 471–498.

Biasi, G. P., R. J. Weldon, T. E. Fumal, and G. G. Seitz (2002), Paleoseismic event dating and the conditional probability of large earthquakes on the southern San Andreas fault, California, *Bull. Seismol. Soc. Am.*, *92*, 2761–2781, doi:10.1785/0120000605.

Branner, J. (1917), The Tejon Pass earthquake of October 22, 1916, *Bull. Seismol. Soc. Am.*, *7*, 51–59.

Crowell, J. C. (2003), Tectonics of Ridge Basin region, southern California, in *Evolution of Ridge Basin, Southern California—An Interplay of Sedimentation and Tectonics*, edited by J. C. Crowell, *Geol. Soc. Am. Spec. Pap.*, 367, 157–203.

Dawson, T., R. Weldon, and G. Biasi (2008), Appendix B: Recurrence interval and event age data for Type A faults, in Working Group on California Earthquake Probabilities (2008), The Uniform California Earthquake Rupture Forecast, Version 2 (UCERF2), *U.S. Geol. Surv. Open File Rep., 2007–1437*, California Geol. Surv. Spec. Rep. 203. [Available at http://pubs.usgs.gov/of/2007/1437/.]

DeLong, S., J. Lienkaemper, A. Pickering, and N. Avdeivitch (2015), Rates and patterns of surface deformation following the South Napa earthquake from laser scanning, *Geosphere*, *11*(6), 2015–2030, doi:10.1130/GES01189.1.

Dingemans, T., S. A. Mensing, S. J. Feakins, M. E. Kirby, and S. R. H. Zimmerman (2014), 3000 years of environmental change at Zaca Lake, California, USA, *Front. Ecol. Evol.*, *2*(34), 1–16, doi:10.3389/fevo.2014.00034.

Dolan, J. F., and T. K. Rockwell (2001), Paleoseismologic evidence for a very large (Mw >7), post-A.D. 1660 surface rupture on the Eastern San Cayetano Fault, Ventura County, California: Was this the elusive source of the damaging 21 December 1812 earthquake?, *Bull. Seismol. Soc. Am.*, *91*(6), 1417–1432, doi:10.1785/0120000602.

Donahue, D. J., T. W. Linick, and A. J. Tull (1990), Isotope-ratio and background corrections for accelerator mass spectrometry radiocarbon measurements, *Radiocarbon*, *32*, 135–142.
Dooley, T. P., and G. Schreurs (2012), Analogue modelling of intraplate strike-slip tectonics: A review and new experimental results, *Tectonophysics*, *574–575*, 1–71, doi:10.1016/j.tecto.2012.05.030.
Duan, B., and D. D. Oglesby (2005), Multicycle dynamics of nonplanar strike-slip faults, *J. Geophys. Res.*, *110*, B03304, doi:10.1029/2004JB003298.
Field, E. H., et al. (2015), Long-term time-dependent probabilities for the Third Uniform California Earthquake Rupture Forecast (UCERF3), *Bull. Seismol. Soc. Am.*, *105*(2A), 511–543, doi:10.1785/0120140093.
Fumal, T. E., R. J. Weldon, G. P. Biasi, T. E. Dawson, G. G. Seitz, W. T. Frost, and D. P. Schwartz (2002), Evidence for large earthquakes on the San Andreas Fault at the Wrightwood, California, paleoseismic site: A.D. 500 to Present, *Bull. Seismol. Soc. Am.*, *92*(7), 2726–2760, doi:10.1785/0120000608.
Goes, S. D. B., and S. N. Ward (1994), Synthetic seismicity for the San Andreas fault, *Ann. Geophys.*, *37*(6), 1495–1513.
Gold, P., M. Oskin, A. Elliot, A. Hinojosa-Corona, M. Taylor, O. Kreylos, and E. Cowgill (2013), Coseismic slip variation assessed from terrestrial lidar scans of the El Mayor-Cucapah surface rupture, *Earth Planet. Sci. Lett.*, *366*, 151–162.
Johnson, K., G. Hilley, and R. Burgmann (2007), Influence of lithosphere viscosity structure on estimates of fault slip rate in the Mojave region of the San Andreas fault system, *J. Geophys. Res.*, *112*, B07408, doi:10.1029/2006JB004842.
Lin, J., and R. S. Stein (2004), Stress triggering in thrust and subduction earthquakes and stress interaction between the southern San Andreas and nearby thrust and strike-slip faults, *J. Geophys. Res.*, *109*, B02303, doi:10.1029/2003JB002607.
Lindvall, S. C., T. K. Rockwell, T. E. Dawson, J. G. Helms, and K. W. Bowman (2002), Evidence for two surface ruptures in the past 500 years on the San Andreas Fault at Frazier Mountain, California, *Bull. Seismol. Soc. Am.*, *92*(7), 2689–2703.
Meltzner, A., and T. Rockwell (2004), The Tejon Pass earthquake of 22 October 1916: An M5.6 event on the Lockwood Valley and San Andreas Faults, Southern California, *Bull. Seismol. Soc. Am.*, *94*, 1293–1304.
Nissen, E., T. Maruyama, J. Arrowsmith, J. Elliot, A. Krishnan, M. Oskin, and S. Saripalli (2014), Coseismic fault zone deformation revealed with differential lidar: Examples from Japanese Mw ~ 7 intraplate earthquakes, *Earth Planet. Sci. Lett.*, *405*, 244–256.
Perrin, C., I. Manighetti, J.-P. Ampuero, F. Cappa, and Y. Gaudemer (2016), Location of largest earthquake slip and fast rupture controlled by along-strike change in fault structural maturity due to fault growth, *J. Geophys. Res. Solid Earth*, *121*, 3666–3685, doi:10.1002/2015JB012671.
Pruitt, A. H., K. M. Scharer, T. E. Fumal, R. J. Weldon, C. L. Gilleland, and R. Sickler (2009), Microgeomorphic reconstruction to determine slip rate on the San Andreas fault near Littlerock, CA, paper presented at SCEC Annual Meeting, Palm Springs, Calif.
Rockwell, T. K., T. E. Dawson, J. Young Ben-Horin, and G. Seitz (2015), A 21-event, 4,000-year history of surface ruptures in the Anza Seismic Gap, San Jacinto Fault, and implications for long-term earthquake production on a major plate boundary fault, *Pure Appl. Geophys.*, *172*(5), 1143–1165, doi:10.1007/s00024-014-0955-z.
Scharer, K., R. Weldon, A. Streig, and T. Fumal (2014), Paleoearthquakes at Frazier Mountain, California delimit extent and frequency of past San Andreas Fault ruptures along 1857 trace, *Geophys. Res. Lett.*, *41*, 4527–4534, doi:10.1002/2014GL060318.
Scharer, K., R. Weldon, and S. Bemis (2016), Testing geomorphology-derived rupture histories against the paleoseismic record of the southern San Andreas fault, paper presented at the 7th International INQUA Meeting on Paleoseismology, Active Tectonics, and Archeoseismology, Crestone, Colo.
Scharer, K. M., R. J. Weldon, T. E. Fumal, and G. P. Biasi (2007), Paleoearthquakes on the southern San Andreas fault, Wrightwood, CA 3000 to 1500 B.C.: A new method for evaluating paleoseismic evidence and earthquake horizons, *Bull. Seismol. Soc. Am.*, *97*(4), 1054–1093, doi:10.1785/0120060137.
Scharer, K. M., G. P. Biasi, R. J. Weldon, and T. E. Fumal (2010), Quasiperiodic recurrence of large earthquakes on the southern San Andreas fault, *Geology*, *38*(6), 555–558, doi:10.1130/G30746.1.
Scharer, K. M., G. P. Biasi, and R. J. Weldon (2011), A reevaluation of the Pallett Creek earthquake chronology based on new AMS radiocarbon dates, San Andreas fault, California, *J. Geophys. Res.*, *116*, B12111, doi:10.1029/2010JB008099.
Scharer, K. M., T. E. Fumal, R. J. Weldon, and A. R. Streig (2014), Photomosaics and event evidence from the Frazier Mountain paleoseismic site, Trench 1, Cuts 1–4, San Andreas Fault Zone, Southern California (2007-2009), *U.S. Geol. Surv. Open File Rep., 2014-1002*, 4 sheets, various scales, pamphlet 23 p. [Available at http://pubs.usgs.gov/of/2014/1002/.]
Scharer, K. M., T. E. Fumal, R. J. Weldon II, and A. R. Streig (2015), Photomosaics and event evidence from the Frazier Mountain paleoseismic site, trench 1, cuts 5–24, San Andreas Fault Zone, southern California (2010–2012), *U.S. Geol. Surv. Open File Rep.*, 25 p., 3 sheets, doi:10.3133/ofr20151147.
Sieh, K. (1978), Slip along the San Andreas fault associated with the great 1857 earthquake, *Bull. Seismol. Soc. Am.*, *68*(5), 1421–1448.
Sieh, K. (1996), The repetition of large-earthquake ruptures, *Proc. Nat. Acad. Sci.*, *93*(9), 3764–3771.
Sieh, K., M. Stuiver, and D. Brillinger (1989), A more precise chronology of earthquakes produced by the San Andreas Fault in southern California, *J. Geophys. Res.*, *94*(B1), 603–623, doi:10.1029/JB094iB01p00603.
Stuiver, M., and H. A. Polach (1977), Discussion: Reporting of 14C data, *Radiocarbon*, *19*, 355–363.
Swanson, B., and B. Olson (2016), Preliminary geologic map of the Frazier Mountain 7.5′ Quadrangle, Kern, Los Angeles, and Ventura Counties, California. California Geological Survey. [Available at http://www.conservation.ca.gov/cgs/rghm/rgm/preliminary_geologic_maps.htm.]
Toppozada, T. R., D. M. Branum, M. S. Reichle, and C. L. Hallstrom (2002), San Andreas Fault zone, California: M ≥5.5 earthquake history, *Bull. Seismol. Soc. Am.*, *92*(7), 2555–2601.
Weldon, R. J., K. M. Scharer, T. E. Fumal, and G. P. Biasi (2004), Wrightwood and the earthquake cycle: What a long recurrence record tells us about how faults work, *GSA Today*, *14*(9), 12–16.
Weldon, R. J., A. R. Streig, and D. Schmidt (2013), Determining slip per event on the San Andreas fault from fold deformation at the Frazier Mountain site, *NEHRP Final Tech. Rep.* [Available at http://earthquake.usgs.gov/research/external/reports/G11AP20123.pdf.]
Wesnousky, S. G. (2008), Displacement and geometrical characteristics of earthquake surface ruptures: Issues and implications for seismic hazard analysis and the process of earthquake rupture, *Bull. Seismol. Soc. Am.*, *98*(4), 1609–1632.
Wu, J. E., K. McClay, P. Whitehouse, and T. Dooley (2009), 4D analogue modelling of transtensional pull-apart basins, *Mar. Pet. Geol.*, *26*(8), 1608–1623, doi:10.1016/j.marpetgeo.2008.06.007.
Zachariasen, J., and T. Dawson (2012), Earthquake chronology on the Big Bend segment of the San Andreas Fault: Filling a gap towards better-constrained rupture scenarios, *NEHRP Final Tech. Rep*. [Available at http://earthquake.usgs.gov/research/external/reports/G08AP00014.pdf.]
Zhou, X. (1990), Tectonic geomorphology and soil chronology of the Frazier Mountain area, Western Transverse Ranges, California, PhD dissertation, Univ. of Calif., Santa Barbara.

Zielke, O., J. R. Arrowsmith, L. G. Ludwig, and S. O. Akçiz (2010), Slip in the 1857 and earlier large earthquakes along the Carrizo Plain, San Andreas Fault, *Science*, *327*(5969), 1119–1122, doi:10.1126/science.1182781.

Zielke, O., J. R. Arrowsmith, L. Grant Ludwig, and S. O. Akciz (2012), High-resolution topography-derived offsets along the 1857 Fort Tejon earthquake rupture trace, San Andreas Fault, *Bull. Seismol. Soc. Am.*, *102*(3), 1135–1154.

Zielke, O., Y. Klinger, and J. R. Arrowsmith (2015), Fault slip and earthquake recurrence along strike-slip faults—Contributions of high-resolution geomorphic data, *Tectonophysics*, *638*, 43–62, doi:10.1016/j.tecto.2014.11.004.